Astronomy & Astrophysics manuscript no. xxlpaperII
December 15, 2015

The XXL Survey ⋆,⋆⋆

II. The bright cluster sample: catalogue and luminosity function

F. Pacaud[1], N. Clerc[2], P. A. Giles[3], C. Adami[4], T. Sadibekova[5], M. Pierre[5], B. J. Maughan[3], M. Lieu[6], J. .P. Le Fèvre[7], S. Alis[8,9], B. Altieri[10], F. Ardila[11], I. Baldry[28], C. Benoist[9], M. Birkinshaw[3], L. Chiappetti[12], J. Démoclès[6,5], D. Eckert[13], A. E. Evrard[14], L. Faccioli[5], F. Gastaldello[12], L. Guennou[15], C. Horellou[17], A. Iovino[18], E. Koulouridis[19,5], V. Le Brun[4], C. Lidman[16], J. Liske[29], S. Maurogordato[9], F. Menanteau[20], M. Owers[21,16], B. Poggianti[22], D. Pomarède[7], E. Pompei[23], T. J. Ponman[6], D. Rapetti[24,25], T. H. Reiprich[1], G. P. Smith[6], R. Tuffs[30], P. Valageas[26], I. Valtchanov[10], J. P. Willis[27], and F. Ziparo[6]

(Affiliations can be found after the references)

Received 3 July 2015 / Accepted 25 November 2015

ABSTRACT

Context. The XXL Survey is the largest survey carried out by the *XMM-Newton* satellite and covers a total area of 50 square degrees distributed over two fields. It primarily aims at investigating the large-scale structures of the Universe using the distribution of galaxy clusters and active galactic nuclei as tracers of the matter distribution. The survey will ultimately uncover several hundreds of galaxy clusters out to a redshift of ~ 2 at a sensitivity of $\sim 10^{-14}$ erg s^{-1}cm^{-2} in the [0.5-2] keV band.

Aims. This article presents the XXL bright cluster sample, a subsample of 100 galaxy clusters selected from the full XXL catalogue by setting a lower limit of 3×10^{-14} erg s^{-1} cm^{-2} on the source flux within a 1′ aperture.

Methods. The selection function was estimated using a mixture of Monte Carlo simulations and analytical recipes that closely reproduce the source selection process. An extensive spectroscopic follow-up provided redshifts for 97 of the 100 clusters. We derived accurate X-ray parameters for all the sources. Scaling relations were self-consistently derived from the same sample in other publications of the series. On this basis, we study the number density, luminosity function, and spatial distribution of the sample.

Results. The bright cluster sample consists of systems with masses between $M_{500} = 7 \times 10^{13}$ and 3×10^{14} $M_{\odot}$, mostly located between z=0.1 and 0.5. The observed sky density of clusters is slightly below the predictions from the WMAP9 model, and significantly below the prediction from the *Planck* 2015 cosmology. In general, within the current uncertainties of the cluster mass calibration, models with higher values of σ_8 and/or Ω_M appear more difficult to accommodate. We provide tight constraints on the cluster differential luminosity function and find no hint of evolution out to $z \sim 1$. We also find strong evidence for the presence of large-scale structures in the XXL bright cluster sample and identify five new superclusters.

Key words. surveys, X-rays: galaxies: clusters, galaxies: clusters: intracluster medium, large-scale structure of Universe, cosmological parameters

1. Introduction

In the current paradigm of cosmological formation of structures, the evolution of dark matter halos results from the competition between gravity and expansion. Following General Relativity, the expansion rate of the universe is governed by its energy content. As the largest bound and virialised entities in the universe, galaxy clusters hold traces of the expansion history. Therefore, provided we are able to estimate their masses reliably, the cluster population constitutes an ideal cosmological 'object' through which to test dark energy models that describe the acceleration of the expansion at late cosmological times (e.g. Weinberg et al. 2013).

Constraining cosmological models requires large samples of galaxy clusters spanning a wide range of masses and redshifts. The principle is to capture the evolution of the halo mass function and the halo spatial distribution across cosmic times. While cluster surveys can be carried out at different wavelengths (Vikhlinin et al. 2009; Mantz et al. 2010; Rozo et al. 2010; Sehgal et al. 2011; Benson et al. 2013; Planck Collaboration et al. 2014, e.g), the X-ray band offers special advantages: (i) X-ray cluster properties can be easily analytically, and self-consistently, predicted by ab initio models and (ii) catalogues are affected to a lesser extent by projection effects. Moreover, medium-depth surveys routinely allow the detection of massive clusters out to $z \sim 1.5$ as well as the systematic inventory of the group-size population at intermediate redshifts. Given that cluster masses are not directly observable quantities, we usually rely on scaling relations based on proxies such as the X-ray temperature or luminosity to determine the cosmologically important halo mass distribution. For the most massive objects, weak-lensing techniques provide independent mass estimates. Because the formation of clusters is essentially gravity driven, it is generally assumed that cluster properties are self-similar as a function

⋆ Based on observations obtained with *XMM-Newton*, an ESA science mission with instruments and contributions directly funded by ESA Member States and NASA. Based on observations made with ESO Telescopes at the La Silla and Paranal Observatories under programme ID 089.A-0666 and LP191.A-0268

⋆⋆ The Master Catalogue is available at the CDS via anonymous ftp to `cdsarc.u-strasbg.fr` (`130.79.128.5`) or via `http://cdsarc.u-strasbg.fr/viz-bin/qcat?J/A+A/vol/page`

of mass, size, and cosmic time (Kaiser 1986). This hypothesis is, however, still a matter of debate, especially for the low-mass objects and needs to be definitively assessed or amended before self-consistent cosmological analyses can be undertaken. In addition, it has been shown (Stanek et al. 2006; Pacaud et al. 2007; Nord et al. 2008) that the determination of the scaling relations requires detailed knowledge of the selection function for the samples in question; a quantity, which is, of course, also mandatory for the final-stage cosmological analysis (Sahlén et al. 2009; Mantz et al. 2010, 2015). The ab initio formalism describing the evolution of the X-ray properties of clusters is also, for the determination of the selection function, an advantage over the other wavelengths. This advantage still holds when performing calculation of the selection function by means of hydrodynamical simulations.

The systematic search for X-ray clusters has a long history, starting from the early times of X-ray astronomy with the pioneering HEAO-1 X-ray observatory (Piccinotti et al. 1982) and the subsequent Einstein Medium Sensitivity Survey (Gioia et al. 1990; Henry et al. 1992). A significant step was achieved by the ROSAT All-Sky Survey (RASS) (Truemper 1993), which provided a wealth of galaxy cluster samples at various depths and completeness levels: REFLEX-I, II (Böhringer et al. 2001, 2014), NORAS (Böhringer et al. 2000), the ROSAT-NEP (Henry et al. 2006), and MACS (Ebeling et al. 2001) to cite only a few of them. At the same time, it was quickly realised that the characterisation of cluster samples strongly benefits from multi-wavelength observations (identification, spectroscopic measurements, and extended calibration of mass-observable relations). With the advent of *XMM-Newton* and *Chandra*, a great effort was devoted to small- and medium-area surveys: COSMOS (Scoville et al. 2007; Finoguenov et al. 2007), XMM-LSS (Pierre et al. 2007), and XMM-BCS (Šuhada et al. 2012), complemented with serendipitous searches: XMM-XCS (Romer et al. 2001; Mehrtens et al. 2012), X-CLASS (Clerc et al. 2012; Sadibekova et al. 2014), and XDCP (Fassbender et al. 2011).

The XXL Survey was designed to bridge the gap between these deep and/or narrow surveys and the RASS. Its ultimate science goal is to provide independent and self-sufficient cosmological constraints, in particular on the dark energy equation of state, before the start of missions covering very large fractions of the sky, such as Spectrum-Roentgen-Gamma (SRG), which will carry the eROSITA instrument, and *Euclid*.

The survey concept is presented by Pierre et al. (2016, hereafter Paper I). It consists of two independent 25 deg^2 fields observed with *XMM-Newton* at a depth of 10 ks leading to the detection of clusters down to $\sim 10^{-14}$ ergs s^{-1}cm^{-2} soft-band flux. Two main aspects received special attention during the design of the survey. The first is the ability to construct a sample containing a few hundred moderately massive clusters, with very well understood selection effects, hence suitable for cosmological studies. While the most massive clusters in the universe have been well identified out to a redshift of about unity, complete samples in the $10^{13} - 10^{14} M_{\odot}$ range are still lacking. The advantage of having a unique extended connected area was also put forward for studies of the large-scale structures. The second aspect is the need for an associated comprehensive multiwavelength follow-up programme with the most advanced ground-based and space observatories. This ensures both internal cross-checks of the selection function and, when possible, a self-consistent determination of the scaling relations for the cluster sample. In addition, the uniform XXL data set enables the systematic assessment of the massive cluster density between redshifts 1 and 2.

The present article is part of the first XXL release based on the data collected during the XMM AO10-11 observing periods. The descriptions of the available X-ray data, their initial processing and quality checks are presented in Paper I together with a thorough description of the project's aims and methods. While some 450 cluster candidates have been inventoried in the XXL Survey to date, we focus here on the 100 brightest objects (hereafter the *bright XXL cluster sample* or the XXL-100-GC sample). This complete sample contains the highest signal-to-noise objects and allows a number of in-depth analyses. We perform various statistical studies of the cluster catalogue in a cosmological context. Complementary results from the same sample are presented in other XXL papers of the first series, in particular: the soft-band luminosity versus temperature scaling relation (Giles et al. 2016, hereafter Paper III) and the quantification of cluster masses using weak lensing (Lieu et al. 2016, hereafter Paper IV).

The paper is organised as follows: Section 2 presents the main steps of the data processing and the requirements imposed on the data quality. Section 3 describes the extraction of the XXL cluster catalogue and the selection of the bright XXL cluster sample from the initial list of XXL extended source candidates. The resulting sample, including spectroscopic redshifts and X-ray luminosities, is presented in Sect. 4. Section 5 describes the derivation of the selection function. The luminosity function, including evolution modelling, is then compared with cosmological models in Sect. 6 and we conclude by a discussion in Sect. 7.

Unless otherwise stated, the results presented in this paper rely on the cosmological parameters measured by Hinshaw et al. (2013), based on the final, nine-year cosmic microwave background (CMB) observations of the Wilkinson Microwave Anisotropy Probe satellite (WMAP), combined with a set of baryon acoustic oscillation (BAO) measurements, and with constraints on H_0 from Cepheids and type Ia supernovae: (H_0 = 69.7 km s^{-1}Mpc^{-1}, Ω_m = 0.282, Ω_Λ = 0.718, σ_8 = 0.817, Ω_b = 0.0461, n_s = 0.9646).

2. Data processing

The full XXL X-ray data set consists of 2.7 Ms of XMM observations from a dedicated AO10-AO11 Very Large Program (VLP), combined with more than 3 Ms of earlier archival observations. After splitting up XMM mosaic mode observations into the relevant individual exposures, 542 XMM pointings are available in total. These are spread over 417 distinct sky positions and in total cover 50.9 deg^2 of the extragalactic sky. We refer the reader to Paper I for a complete description of the survey layout and design.

The raw data were re-processed using recent calibration information and `XMM-SAS` version 10.0.2. Periods of high radiation level or particle contamination were identified and filtered out from broadband ([0.3-10] keV) light curves, as proposed by Kuntz & Snowden (2008). Following Pratt & Arnaud (2002), a histogram of the light curve values was fitted with a Poisson law for each camera and the time intervals falling outside the $\pm 3\sigma$ range were excluded.

Images, exposure maps and detector masks in several bands were then generated from the filtered event-lists and telescope attitude using 2.5″pixels and were processed with the XMM-LSS/XXL source detection pipeline, Xamin (Pacaud et al. 2006; Clerc et al. 2012), which we briefly summarise below. The raw images were filtered in wavelet space using the method described by Starck & Pierre (1998), which combines a rigorous treatment of the Poisson noise in low intensity signal with an iter-

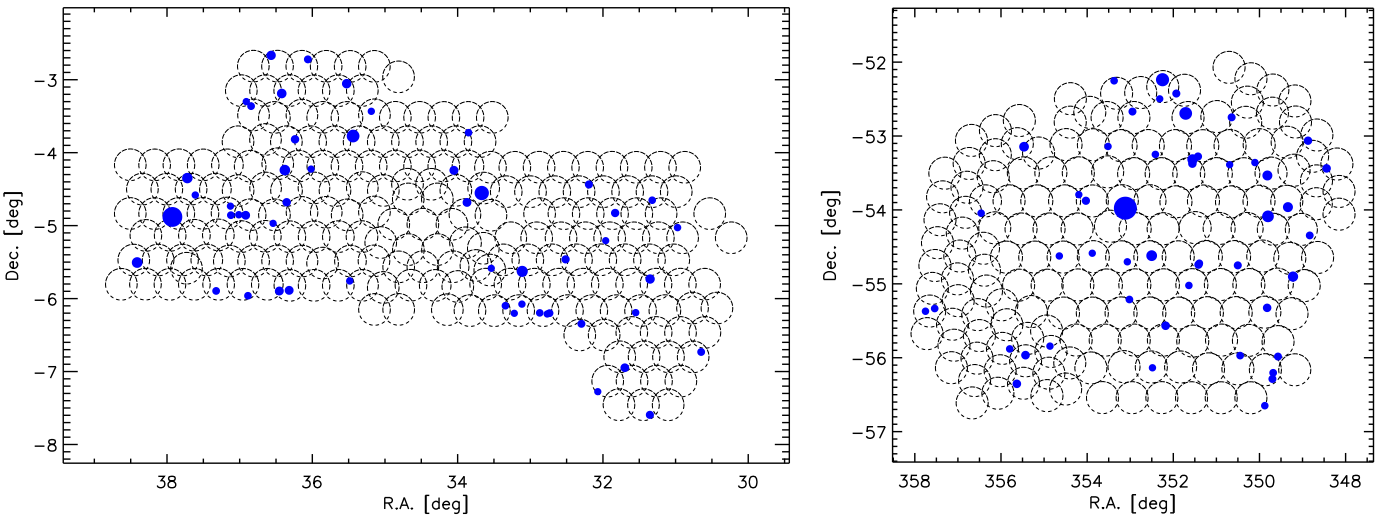

Fig. 1. Sky distribution of the XXL pointings that passed the selection criteria for the construction of the cluster sample. The dashed circles represent the area used for cluster detection on each pointing, i.e. a 13′ radius around the average optical axis. The location of the members of the bright XXL cluster sample is shown with blue dots, whose size is proportional to their 60″ aperture flux. The ∼ 1 deg^2 area located around RA=34.5 and Dec =-5, is the Subaru Deep Survey, whose position was selected for its lack of bright X-ray sources.

ative image reconstruction process that prevents flux loss. We then ran SExtractor (Bertin & Arnouts 1996) with a low detection threshold on the filtered images to extract a conservative source catalogue and generate source masks. Finally, a dedicated XMM maximum likelihood fitting procedure was used to determine morphological parameters and flux for the source candidates, together with likelihood ratios to assess the detection and source extent probabilities.

Given that a number of sky positions have been observed several times, usually because of high flaring rates, we generated pseudo pointings by co-adding the images and exposure maps of all suitable (possibly truncated) pointings at a given location; for the great majority, there is only one relevant pointing per position. The decision as to which pointings should enter a given stack was taken by optimising the average signal-to-noise achieved in a 1′aperture. The bright XXL cluster sample was defined based on the Xamin catalogues of 412 stacks. Indeed, 5 of the 417 sky positions correspond to pointed follow-up observations of XMM-LSS/XXL clusters which fully overlap genuine survey pointings. These were excluded from the source extraction process to avoid selection biases.

Despite the overall good homogeneity of the XXL data set, we observe variations in the quality of the different stacks - this is particularly noticeable in the areas covered by the AO10-AO11 VLP since most of the sky positions have been observed only once. We ran extensive quality checks in order to filter out observations that are not suitable for the subsequent derivation of the selection function. These checks are discussed in detail in Paper I. This results in two limits: stacks with less than 3 ks of clean observing time (18 of them) were not considered useful owing to their strong initial contamination, poor depth, and the difficulty to assess the background properties; high-background pointings (>4.5 ct/s/pointing in the [0.5-2] keV band) were also rejected since the modelling of the selection function would become uncertain for low surface brightness sources. This results in a subselection of 386 stacks. Considering only the innermost 13′ of each pointing, the survey covers a total geometric area of 46.6 deg^2 at high galactic latitudes (24.4 deg^2 in the north and 22.2 deg^2 in the south). The selected pointings and the corresponding (geometric) sky coverage are shown in Fig. 1. The figure also shows the lower density of pointings in the southern field resulting from the larger spacings used for the preliminary XMM-BCS Survey (Šuhada et al. 2012). This, combined with the smaller total sky area, results in a lower sky coverage for the southern field.

3. Sample selection

3.1. The full XXL cluster sample

Extended source candidates are selected from the Xamin maximum likelihood outputs in the `extent` / `extent_likelihood` / `detection_likelihood` 3D space (Pacaud et al. 2006). By default, all sources with measured `extent` greater than 5″ and `extent_likelihood` greater than 15 are considered as extended. Among these, we differentiate a high significance sample – the C1 class with an `extent_likelihood` greater than 33 and a `detection_likelihood` greater than 32 – from the remaining candidates, which we term the C2 class. The C1 sample has proven to be mostly free of contamination by spurious detections or blended point sources both from simulation (Pacaud et al. 2006; Clerc et al. 2012) and observations (Pacaud et al. 2007; Clerc et al. 2014). In comparison, the C2 population is about 50% contaminated (Pierre et al. 2006; Adami et al. 2011).

For typical XMM cluster extents – a core radius of 20″ – and nominal XXL observing conditions, the C1 and C2 classes correspond to flux limits of $\sim 2 \times 10^{-14}$ erg s^{-1} cm^{-2}and $\sim 8 \times 10^{-15}$ erg s^{-1} cm^{-2}, respectively. However, strictly speaking, the Xamin selection is a non-straightforward function of both cluster flux and extent, as shown by Pacaud et al. (2006) and Clerc et al. (2012). These aspects are discussed in more detail in Sect. 5.

Cluster substructures and multiple detections on neighbouring pointings have been cross-identified with a 2′search radius and controlled by a human moderator before removal. In doing so, we prioritised detections with the lowest off-axis angle.

3.2. Identifying the hundred brightest XXL clusters

The initial inventory of the XXL source population indicates that the cluster cosmology sample will ultimately contain approximately 500 clusters of galaxies. The spectroscopic validation of such a large sample of cluster candidates is a long process, especially tedious at high redshift. As of April 2015 (two years after the completion of the XMM observations), spectroscopic or photometric redshifts have been determined for ∼ 85% of the ∼ 450 X-ray cluster detections to date.

For the first set of scientific studies, we focus on a complete subsample of the brightest XXL clusters so as to enable statistical studies of cluster physics for the group-mass range at intermediate redshifts (i.e. for the dominant population of the survey) along with a preliminary cosmological analysis. This sample will allow the most detailed X-ray analyses for the XXL cluster population and is intended to stand as a benchmark for all future studies.

We decided to set the size of the bright XXL cluster sample to 100 objects and opted for a flux-limit selection in a fixed angular aperture. Such a model-independent procedure ensures that the selection is easily reproducible by alternative processings. The goal was to select a homogeneous set of clusters with at least 100 X-ray counts in a high signal-to-noise area, taking into account the sensitivity drop of about 1/2 due to the vignetting at the edge of the XMM field of view. It also minimises the impact of the initial C2 selection since we only consider the most prominent objects in the survey in terms of surface brightness. This was confirmed a posteriori by the fact that most of the clusters in the final sample are classified as C1.

This high-flux selection effectively limits the bright sample to redshift of $z \sim 1$, while 1-2 clusters per deg^2 are expected beyond redshift of unity in XXL (Pierre et al. 2011). These clusters will not be used in the initial XXL cosmological studies: current uncertainties on cluster evolution have a critical impact on the modelling of the selection function of these objects and of their physical properties. Rather, the distant cluster sample is undergoing dedicated multiwavelength studies that will characterise their properties more accurately and will permit to develop procedures that lead to reliable mass estimates.

To select the brightest sources, we start from the cleaned C1+2 source list (i.e. the union of the C1 and C2 clusters), for which the Xamin pipeline provides angular core radius (θ_c) and total flux estimates from a fit with a $\beta = 2/3$ surface brightness model (Cavaliere & Fusco-Femiano 1976). This enables us to derive approximate count rates within a given radius. A preliminary step was to select the 184 brightest clusters from the current XXL C1+2 catalogue. This pre-selection was based on pipeline total count rates in the [0.5-2] keV band, integrated out to a fixed angular radius of 60″; this radius was chosen to encompass a significant fraction of the cluster emission at all distances (a cluster core radius of 180 kpc ranges from 100 to 23″for $0.1 < z < 1$). Only clusters with a total pipeline count rate above 0.025 cts/s in the aperture were retained. Subsequently, the aperture photometry of every cluster from this primary selection was re-evaluated using a growth curve analysis (GCA) as described by Clerc et al. (2012). In particular, nearby-source masking, cluster centring and the local background estimate were interactively optimised; one example is shown in Fig. 2. This finally allowed us to select the 100 brightest XXL clusters within a 60″flux aperture. In the process, we assume that there is a one-to-one correspondence between count rate and flux and so we ignore the temperature dependence of the energy-to-flux conversion factor (ECF). This is necessary since some sources were not observed by one of the detectors, either because of a misalignment of the MOS and PN detectors or because some of the MOS1 CCDs are switched off in recent observations. The flux selection can therefore be considered as a count rate limit, in which average ECFs were used to extrapolate the information for missing detectors. The assumption of a fixed ECF has little impact in practice, since the cluster selection operates in the narrow [0.5-2] keV band where the XMM effective area curve shows little variation over typical cluster spectra. By iteratively comparing the 60″count rates from the pipeline output and from the growth curve analysis, we estimate that the sample defined in this way is more than 99% complete, for the initial pre-selection of 184 clusters. However, uncertainties on count rate measurements from the growth curve analysis (typically 15 % at the faint end of the sample) render the selection limit of the faint objects somewhat fuzzy. Given the count rate distribution of the pre-selection, this concerns about 20 clusters just above and below the selection threshold which are randomly reshuffled. Therefore, a model of the selection function must include the measurement errors arising from the growth curve analysis.

The flux limit of the final catalogue is $3{\times}10^{-14}$ erg s^{-1} cm^{-2} in a 60″ radius aperture; this is equivalent to a total MOS1+MOS2+PN count rate of 0.0332 cts/s in [0.5-2] keV, with the assumed ECF of 1.107×10^{12} cts erg^{-1}cm^{-2}[1].

4. The catalogue

The bright XXL cluster sample consists of 96 C1 and 4 C2 clusters, almost equally distributed between the two XXL fields: 51 in XXL-N and 49 in XXL-S. The clusters and their main parameters are presented in Table D.1. In addition, seven additional clusters above the flux limit were identified but not included in the sample: five that were detected in the bad quality stacks and two that did not pass the pipeline C1+C2 selection criteria. These clusters are listed in Table D.2 for completeness, but they will not be used in the scientific analysis presented here. Some members of the bright XXL cluster sample are already known from previous works: 22 of them are in the initial XMM-LSS area (Clerc et al. 2014), 13 in the initial BCS X-ray sample (Šuhada et al. 2012), and 12 from other projects (including the ROSAT All-Sky Survey and optical surveys).

4.1. Cluster redshift validation

The determination and validation of the cluster redshifts is an important part of the XXL Survey effort necessary to reach the full survey scientific potential. Obtaining spectroscopic redshift for several hundred clusters out to a redshift of 1 and beyond is nevertheless a long-term process involving numerous observing facilities, hence requiring a dedicated management and substantial manpower.

In the first step, we used the CFHTLS T0007[2] and BCS (Menanteau et al. 2010) photometric redshift catalogues to assign preliminary cluster redshifts; the procedure looks for a galaxy overdensity in redshift-space around the X-ray centroid. Subsequent spectroscopy has shown that the CFHTLS and BCS estimates have errors < 0.08 and 0.12, respectively, for 99 % of the clusters; these precisions are valid up to $z \sim 1$.

[1] All conversion from luminosities to count rates or fluxes in this paper use an average n_H column density over the two XXL fields of 1.8×10^{20} cm^{-2}.

[2] http://www.cfht.hawaii.edu/Science/CFHTLS/T0007/

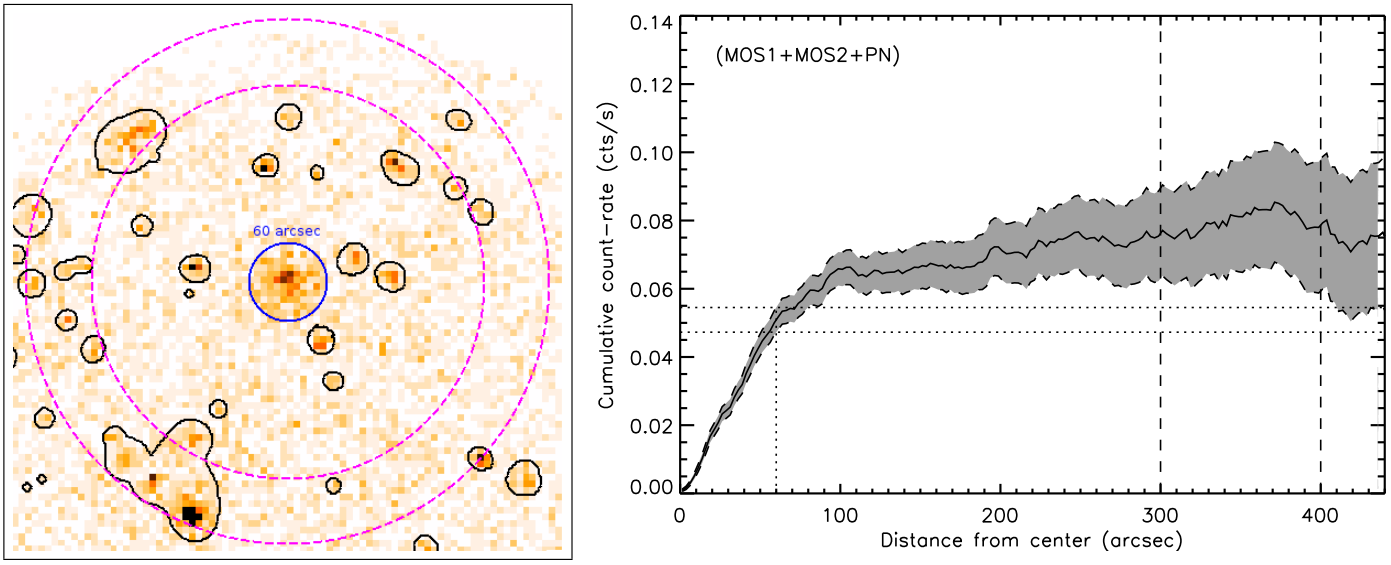

Fig. 2. Growth curve analysis of galaxy cluster XLSSC 010 at $z = 0.33$. The 60″aperture flux of this cluster is close to the median value in the bright XXL cluster sample. *Left*: Source masking is shown by the black lines. The two dashed pink circles delimit the annulus used for the background estimate. The cluster selection was made from the integrated [0.5-2] keV count rate measured within a radius of 60″(blue line). *Right*: Growth curve of XLSSC 010. The grey area represents the 1-σ confidence interval. The dotted lines show the 60″extraction radius (vertical line) and the corresponding 1-σ interval for the aperture count rate (horizontal lines). The dashed vertical lines indicate the radial range within which the background was estimated.

As described in Paper I, a comprehensive follow-up programme has been tailored in order to obtain spectroscopic redshifts (and, possibly, velocity dispersions) for all XXL clusters and for a significant and representative fraction of the active galactic nucleus (AGN) population. The enterprise involves already available redshifts from external programmes, like VIPERS (Garilli et al. 2014) or GAMA (Driver et al. 2011), as well as from dedicated XXL follow-up campaigns at ESO (Large Programme), Anglo-Australian Telescope (Lidman et al. 2016, hereafter Paper XIV), William Herschel Telescope (Koulouridis et al. 2016, hereafter Paper XII), and others. We refer to our dedicated website[3], for detailed and regularly updated information on the XXL follow-up activities. All available spectra in both areas along with redshift values, measurement errors and quality flags are stored in the CESAM database in Marseille[4], from which the spectroscopic identification of the X-ray sources is performed. For clusters of galaxies, we follow here the procedure developed for the XMM-LSS survey (Adami et al. 2011). This task is conducted mostly in interactive mode and undergoes independent checks by at least two moderators. We assume that a cluster is spectroscopically confirmed either i) when there are three concordant redshifts within a radius of 500 kpc from the X-ray centroid or ii) when at least the cD galaxy has a spectroscopic redshift, taking into account the preliminary information provided by the photometric redshift analysis. For the vast majority of the bright XXL cluster sample, the spectroscopic identification was straightforward; in some cases, where for example a cluster is undergoing a merger event or two velocity groups are superposed along the line of sight, a human decision was necessary; these very few cases are documented in Appendix A. The origin of the redshifts of the bright XXL cluster sample is shown in Fig. 3. At the time of paper submission, all clusters but three have been spectroscopically confirmed; the remaining ones are scheduled for the next ESO observing periods (Large Programme by C. Adami). For these few objects we still use the photometric redshift estimates for the first series of XXL papers (see Table D.1).

The redshift distribution of the bright XXL cluster sample is shown in Fig. 4. It is very similar, within the statistical noise, to the distribution of the total set of currently confirmed XXL clusters, which is ∼2.5 times larger. This probably results from our choice of a fixed angular aperture for the flux cut, which favours the inclusion of the more compact high redshift clusters despite their lower average total flux.

The cluster density is similar in the two XXL fields. Despite the slightly larger area and deeper exposure in the north (see Paper I and Sect. 2), we observe marginally higher numbers in the southern field. The deviations are, however, always within the expectations from shot noise. Interestingly, the redshift distribution of both the bright XXL cluster sample and the currently confirmed XXL clusters do not seem to reproduce the deficit of clusters at redshifts of $0.4 < z < 0.6$ previously reported by Clerc et al. (2014), who studied a subsample of the full XXL C1 catalogues. Either this lack of clusters was simply the result of cosmic variance, or it results from a deficit of low-mass systems below the flux limit imposed in the present work.

4.2. Cluster X-ray properties

The clusters underwent a detailed X-ray spectroscopic analysis, which is extensively described in Paper III. Briefly, XMM spectra were extracted for all the available detectors in a fixed 300 kpc circular aperture around the pipeline position. The background was modelled, for each XMM instrument, using an annulus encompassing the same off-axis range as the source aperture. When the source was too close to the centre, a surrounding annulus was used instead. The spectra were fitted with a thermal emission model including absorption by Galactic neutral hydrogen (Kalberla et al. 2005). Since the metallicity could only be constrained for a few systems, we fixed it to $0.3 Z_{\odot}$ for all clusters to ensure self-consistency. In addition to the spec-

[3] http://xxlmultiwave.pbworks.com
[4] http://cesam.lam.fr/xmm-lss/

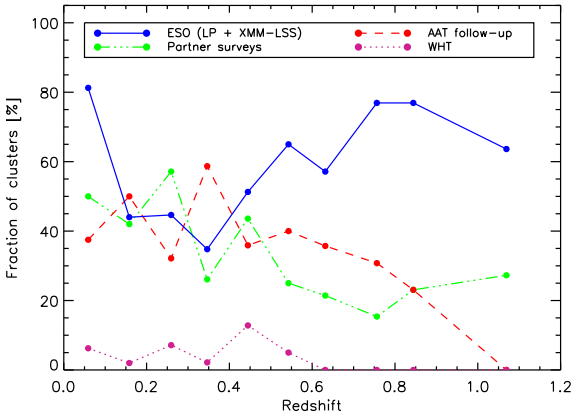

Fig. 3. Origin of the XXL-100-GC sample spectroscopic redshifts in different redshift slices. The available spectroscopic data are split into four categories: (i) the follow-up data obtained by the dedicated XXL ESO Large Program (LP, PI: C. Adami) using a combination of NTT/EFOSC2 and VLT/FORS2, together with previous data obtained by the XMM-LSS team with the same instruments, (ii) the XXL follow-up program based on the the Anglo-Australian Telescope (AAT, PI: C. Lidman), (iii) the XXL William Herschel Telescope (WHT) follow-up program (PI: B. Poggianti), and (iv) redshifts obtained through partner spectroscopic surveys, including GAMA (Driver et al. 2011), VIPERS (Garilli et al. 2014) and the VVDS (Le Fèvre et al. 2013). The observations and data reduction for the redshifts obtained at the WHT and AAT are respectively the subject of XXL Paper XII and Paper XIV. For each category, the plot shows the proportion of clusters with galaxy redshifts coming from the corresponding project.

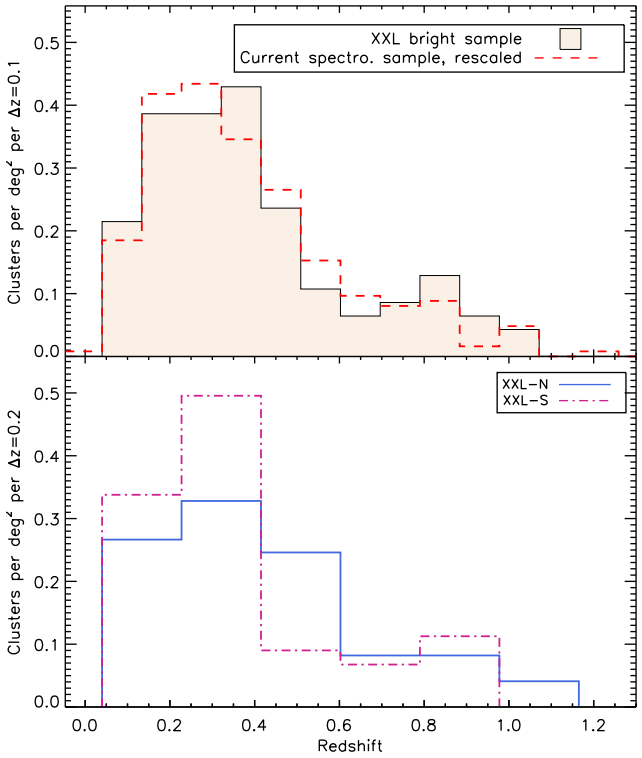

Fig. 4. Redshift distribution of the bright XXL cluster sample. Top: The bright sample compared with the distribution of 267 spectroscopically confirmed XXL clusters (to date). The latter has been rescaled to the same total number. Bottom: North/south fields separately (the bin width was doubled to obtain a shot noise comparable to that of the complete histogram).

troscopically weighted temperature, $T_{300\ \mathrm{kpc}}$, the rest frame [0.5-2] keV luminosity $L^{\mathrm{XXL}}_{300\ \mathrm{kpc}}$ in the extraction region was derived as part of the fit and corrected for the masked areas. To obtain physically meaningful luminosities, we estimated $r_{500,\mathrm{MT}}$ and $M_{500,\mathrm{MT}}$[5] from the best fit temperatures and the average $M_{500,\mathrm{WL}} - T_{300\ \mathrm{kpc}}$ scaling relation derived in Paper IV from a weak lensing analysis of the XXL-100-GC sample clusters overlapping the CFHTLenS area (Erben et al. 2013) combined with clusters from the Canadian Cluster Comparison Project (Hoekstra et al. 2015). The parameters of this scaling relation are given in Table 1. The values of $L^{\mathrm{XXL}}_{300\ \mathrm{kpc}}$ were then extrapolated to $r_{500,\mathrm{MT}}$ using, for consistency, the same β-model as for the selection function modelling (see Sect. 5).

The resulting cluster luminosities and masses within $r_{500,\mathrm{MT}}$, $(L^{\mathrm{XXL}}_{500,MT}, M_{500,\mathrm{MT}})$ are listed in Tables D.1-D.2. The quoted errors on cluster masses combine the uncertainty on the cluster temperatures with the intrinsic scatter of the $M_{500,\mathrm{WL}} - T_{300\ \mathrm{kpc}}$ relation but do not include the uncertainty on the scaling relation parameters (again for consistency with the selection model). However, the corresponding errors on $r_{500,\mathrm{MT}}$ are not propagated to $L^{\mathrm{XXL}}_{500,MT}$ (but the effect is small).

Figure 5 shows the distribution of the bright XXL cluster sample in the (z, L_X) plane, revealing the usual Malmquist bias of flux/magnitude-limited samples. The figure also shows the lack of massive clusters at low redshift resulting from volume effects, implying that the sample shows a strong mass versus redshift correlation. This correlation increases the degeneracy between the redshift evolution and the other parameters in the self-consistent scaling relation analysis based on the XXL clusters alone. Such errors propagate straight into the cosmological analysis of the sample, as we will show later. We note, however, that the correlation will become milder with the full XXL cluster sample as we add lower luminosity clusters at all redshifts.

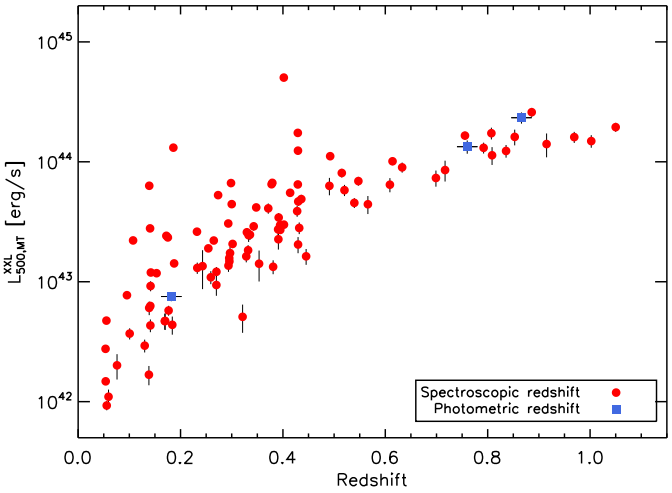

Fig. 5. Distribution of the bright XXL cluster sample in the $L^{\mathrm{XXL}}_{500,MT}$ vs redshift plane. The luminosity is measured in the [0.5-2] keV band and integrated to $r_{500,\mathrm{MT}}$. The data show a clear Malmquist bias due to the flux selection combined with volume effects that prevent us from detecting massive (and thus luminous) clusters at low redshift.

The mass distribution of the sample is illustrated in Fig. 6. Surprisingly, the high redshift part of the sample (≃40% of the total) covers a narrow range in cluster masses

[5] The radius within which the average total mass density of the cluster equals 500 times the critical density estimated at the cluster redshift, and the total mass within this radius.

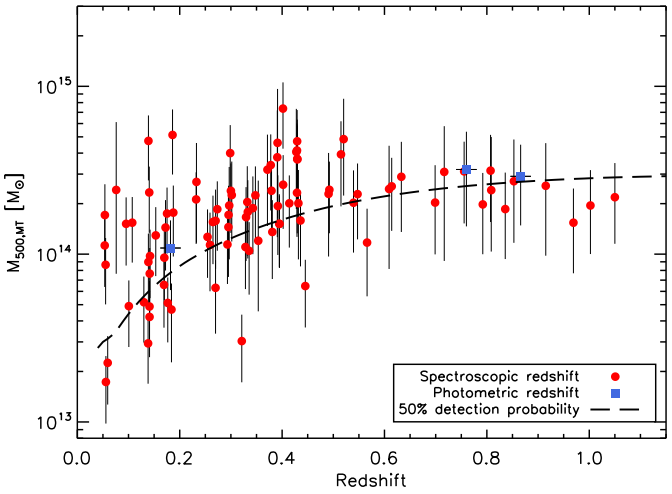

Fig. 6. Distribution of the bright XXL cluster sample in the $M_{500,MT}$ vs redshift plane. Although many low mass systems are detected at low redshift ($\sim$ 20% of the sample with $M_{500,MT} < \times 10^{14}\,M_\odot$), the high redshift subsample mostly contains similar mass clusters. The dashed line shows the 50% completeness limit in the WMAP9 cosmology from the model described in Sect. 6.1.

($M_{500,MT} = 2{-}3 \times 10^{14}\,M_\odot$). We point out that this is not a direct consequence of picking up clusters with similar luminosities (close to the detection limit) at high z since the $M_{500,\rm MT}$ estimates are derived from the measured temperatures rather than luminosities. Instead, it likely results from a subtle balance between the evolution of the cluster number density, the evolution of scaling laws and the apparent sizes of clusters.

In Fig. 8, we compare the distribution of the XXL-100-GC clusters in mass and redshift with samples extracted from different surveys. The XXL-100-GC sample probes lower masses than most previous ICM-based cluster surveys. The 400d survey (Burenin et al. 2007) stands as an example of projects that rely on deep archival ROSAT pointings. For consistency, we estimated the cluster masses from their measured temperature combined with the XXL $M_{500,\rm WL} - T_{300\ \rm kpc}$ scaling relation of Paper IV. ROSAT surveys do not exhibit the flat mass selection observed at high redshift in the XXL-100-GC sample. We also show the largest samples selected from the Sunyaev-Zel'dovich effect (SZE) with the South Pole Telescope (Bleem et al. 2015, SPT,) and the *Planck* satellite (Planck Collaboration et al. 2015a). For these data, we relied on the masses derived from scaling relations between M_{500} and the SZE signal by each of the teams. A few XXL clusters correspond to SZE detected massive systems. They are listed in the individual notes of Appendix A and reveal a good agreement between the $M_{500,\rm WL} - T_{300\ \rm kpc}$ based masses obtained in this work and estimates based on the SZE.

Clearly, the XXL-100-GC sample probes lower masses than most previous ICM-based cluster samples, including those selected from deep ROSAT pointed observations. The full XXL sample will go even deeper and will uncover a new, little-studied, high redshift, and low mass cluster population.

5. Selection function

The bright XXL cluster sample relies on the initial C1+2 selection combined with a later flux cut. Given the high subsequent flux cut, one would expect the C1+2 incompleteness to have little impact on the final selection function. However, there is still a residual effect, which causes very extended sources to be detected less efficiently or compact sources to be mistaken for point sources. In addition, the flux measurement errors of the GCA ($\sim$15% near the threshold) play an important role in the selection process and depend on the local exposure time (and therefore the pointing on which the source was detected). Finally, the estimate of the completeness in regions where several pointings overlap must exactly follow the order and manner in which the two selection steps are applied to the source candidates.

In this section we describe a solution to each of these problems and discuss the resulting XXL-100-GC sample selection function.

5.1. Pipeline selection function

The C1+2 selection has been studied in depth in previous works, using simulations of β-model clusters (e.g. Pacaud et al. 2006). In this work we follow the methodolgy of Clerc et al. (2012), where clusters are simulated in synthetic observations with variable exposure time, t_{exp}, and particle background level, adding AGNs as a spatially uncorrelated point-source distribution that follows the flux distribution of Moretti et al. (2002). For the background, we take as nominal values the average sky emission and XMM instrumental background measured by Read & Ponman (2003), and allow for a variable particle background level by applying a rescaling factor, b, to the instrumental background. For each set of β-model parameters, the C1+2 selection function was then estimated in four off-axis angle bins (0–4′, 4–7′, 7–10′ and 10-13′) and for several values of the exposure time and background level in the range $3\,\rm ks < t_{exp} < 40\,ks$ and $0.25 < b < 4$.

In practice, evaluating the average exposure time of a given pointing is straightforward, but this is not as trivial for the background parameter. To estimate b, we use a least-square matching procedure that compares the background measured by the XAMIN pipeline at the position of each detected source to the one derived at a similar off-axis angles in simulations with different values of b. We then interpolate the selection functions to the proper b and t_{exp} for each pointing.

Although the β-model cluster profiles are a function of both r_c and β, we showed in Pacaud et al. (2007) that the C1+2 selection mostly depends on the width of the profile (e.g. FWHM) and the flux in the central parts. Since all the analysis in the following relies on the flux within 60″or $r_{500,\rm MT}$ and ignores the contribution from the cluster outskirts, the impact of β on the selection is dominated by the degeneracy between β and r_c. We therefore fix β to a canonical value of 2/3 in the remaining. For each value of b and t_{exp}, the C1+2 detection probability is estimated for core radii in the range 10″$< r_c <$100″and total XMM count rates (summed over the three detectors and integrated to infinite radius) spanning 0.0025 ct/s$< CR_\infty <$0.5 ct/s.

From here on, we denote the pipeline selection function in pointing p, i.e. the probability of inclusion in the sample, as $P_{C1+2,p}\,(I|CR_\infty, r_c, RA, Dec)$, where the dependence on t_{exp} and b is encapsulated in the pointing under consideration and the off-axis angle is implicitly given by the sky position.

5.2. Modelling the flux cut

While a simple limit on the aperture flux would be easy to implement, it would not accurately reproduce the XXL-100-GC selection process since the GCA photometry is affected by noise.

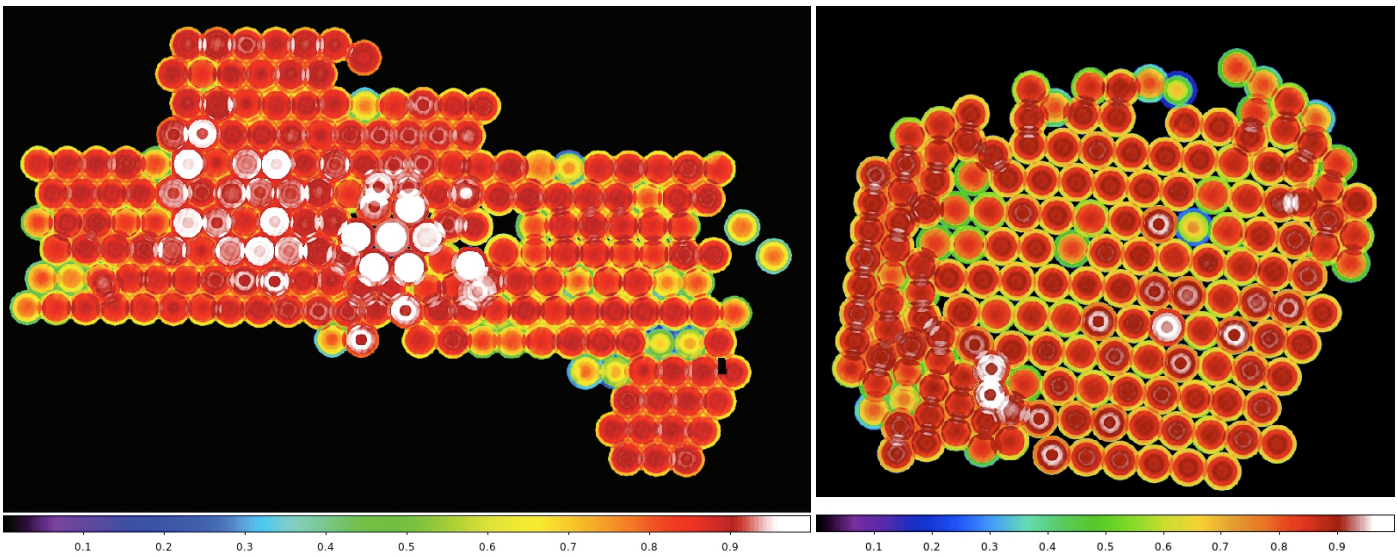

Fig. 7. Detection efficiency map for a cluster with a core radius r_c=20″and a total XMM count-rate (integrated to infinity) of CR_∞=0.055 cts/s. The maps include the effect of the initial C1+2 selection, the subsequent aperture flux cut with its measurement error, and the combination of overlapping pointings.

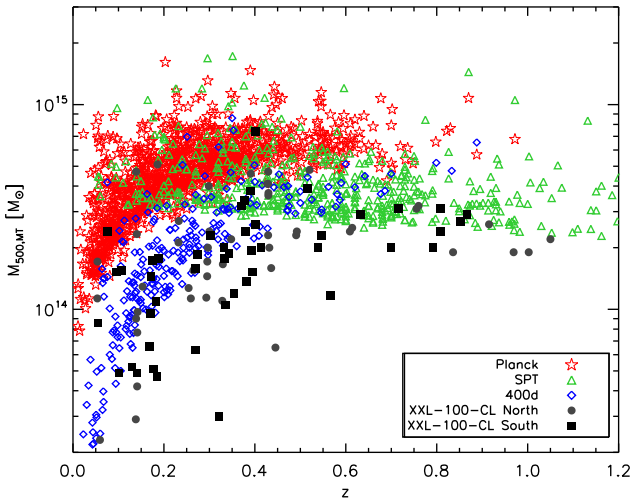

Fig. 8. Comparison of the mass and redshift distribution of the bright XXL cluster sample with other cluster samples. We detect on average lower-mass / higher-redshift clusters than current Sunyaev-Zel'dovich cluster surveys (Bleem et al. 2015; Planck Collaboration et al. 2015a), as well as the 400 deg^2 ROSAT survey based on deep archival pointings. At high redshift, the selection of the XXL-100-GC sample is also much closer to being mass-limited than for ROSAT-based surveys such as the 400d.

A proper understanding of the count rate measurement errors is therefore necessary.

Actually, a simple Poisson approximation (which ignores the subtle effects of background estimation, correction for masked areas and varying exposure) proved sufficient to reproduce the measured errors for the 100 observed clusters. In this model, we generate a counts image by distributing the count rate uniformly within the 60″ aperture, multipling by the exposure map and adding a modelled background. The Poisson error on the count rate is simply obtained from the total counts in the aperture and a global rescaling by the average exposure time in the aperture. This provides us with maps of the GCA measurement errors for different source fluxes and positions. Since these error maps are tailor-made for each pointing, they naturally account for gaps and missing MOS CCDs in addition to the local exposure time and background level.

As we always have more than 50 photons in the 60" aperture, the Poisson error on the aperture counts is close to a Gaussian distribution. For simplicity, we assume that the same holds for all other sources of uncertainty (e.g. background estimation, correction for varying exposure in the aperture). In this case, the probability of exceeding the count rate cut CR_{cut} for a source with a true aperture flux CR_{60} given the local measurement error $\sigma_m\,(CR_{60}, RA, Dec)$ is

$$P_{cut}\,(I|CR_{60}, RA, Dec) = \frac{1}{2}\left(1 + \mathrm{erf}\left[\frac{CR_{60} - CR_{cut}}{\sigma_m\,(CR_{60}, RA, Dec)\,\sqrt{2}}\right]\right). \quad (1)$$

Including the pipeline C1+2 incompleteness, the exact selection of the bright XXL cluster sample becomes, for a single pointing p_i,

$$P_{p_i}\,(I|CR_\infty, r_c, RA, Dec) = \frac{P_{C1+2,\,p_i}\,(I|CR_\infty, r_c, RA, Dec)}{2} \times \left(1 + \mathrm{erf}\left[\frac{\epsilon_{60}(r_c)CR_\infty - CR_{cut}}{\sigma_m\,(\epsilon_{60}(r_c)CR_\infty, RA, Dec)\,\sqrt{2}}\right]\right), \quad (2)$$

where CR_∞ is the total β-model flux (integrated to infinity) and $\epsilon_{60}(r_c) = \left(1 - \left[1 + (60"/r_c)^2\right]^{1.5-3\beta}\right)$ is the fraction of this flux included in the 1′ aperture.

5.3. Pointing overlaps

Modelling the effect of pointing overlaps would be straightfoward if the XXL-100-GC sample was just the union of independent cluster catalogues from different pointings. The probability of not detecting a source on any pointing would simply be the product of the non-detection probabilities on all available pointings. This is, for instance, the case for the completeness of the full C1+2 sample provided by the XXL detection pipeline,

$$P_{C1+2}\,(I) = 1 - \prod_{i=1}^{N}\left[1 - P_{C1+2,p_i}\,(I)\right], \quad (3)$$

where we temporarily dropped the dependence on CR_∞, r_c and position (RA, Dec) for brevity.

Such a simple prescription does not apply to the bright XXL cluster sample, for which the whole selection process was not repeated independently over each pointing. Instead, we first assembled the union of C1+2 detections on the different pointings and then ran the GCA only once per cluster on the good pointing where it was detected with the lowest off-axis angle. In this case, the combined selection function reads

$$P(I) = \sum_{i=1}^{N} \left(P_{p_i}(I) \prod_{j<i} \left[1 - P_{C1+2,p_j}(I) \right] \right), \quad (4)$$

where the N pointings in the summation and product must be ordered by the off-axis angle for the position under consideration. This effectively accounts for the flux cut on a given pointing p_i only if the cluster has not been detected in any pointing p_j with a lower off-axis angle ($j < i$).

For each value of CR_∞ and r_c, we generated a 2D completeness map based on Eq. (4). Examples of such maps for a typical cluster count rate and core radius are shown in Fig. 7. In these maps, the spatial variation of the detection efficiency mainly reflects the local exposure time. This is a result of the stringent selection on background level imposed for the construction of the sample, while we use a wide range of exposures from 3 ks in the shallowest dedicated XXL observations to 80 ks in the Subaru/XMM Deep Survey (Ueda et al. 2008), which is part of the northern field.

5.4. Sky coverage

For most applications, the full 2D selection function is not required. The sky coverage of the sample is straightforwardly derived from the sensitivity maps as

$$\Omega_S(CR_\infty, r_c) = \int P(I|CR_\infty, r_c, RA, Dec)\, d\Omega. \quad (5)$$

The resulting selection function for the XXL-100-GC sample is shown in Fig. 9. This figure captures the impact of each step of the selection process: the thick dashed curve corresponds to the fixed 60″flux cut of 3×10^{-14}erg s^{-1} cm^{-2}, while the transition between this line and the 1deg^2 area curve shows the spread around the cut due to measurement errors in the GCA. Finally, the modulations at large core radii and for count rates exceeding the flux cut reflect the initial C1+C2 selection function.

A more accurate visualisation of the selection function is provided in the left panel of Fig. 10 which shows slices of the sky coverage at constant core radius, as a function of count rate. The faint-end part of each curve for $10'' < r_c < 50''$results from the XXL-100-GC sample flux cut broadened by measurement uncertainties, while additional pipeline selection alters the detection efficiency at larger radii and fluxes.

The relative contribution of the two fields to the total sky coverage is shown in the right panel of Fig. 10. For the faintest sources, the sky coverage is much larger in the north due to the existence of a few deep areas like the Subaru/XMM deep Survey (Ueda et al. 2008). At larger count rates, however, the sky coverage is 10 to 15% larger in the northern field as expected from the geometry of the survey.

6. Cosmological analysis

In this section we analyze the distributions of the XXL-100-GC sample in both luminosity and position on the sky, and compare these distributions with the predictions of the baseline WMAP9 cosmological model, with masses converted to X-ray luminosities via the scaling relations from papers III and IV.

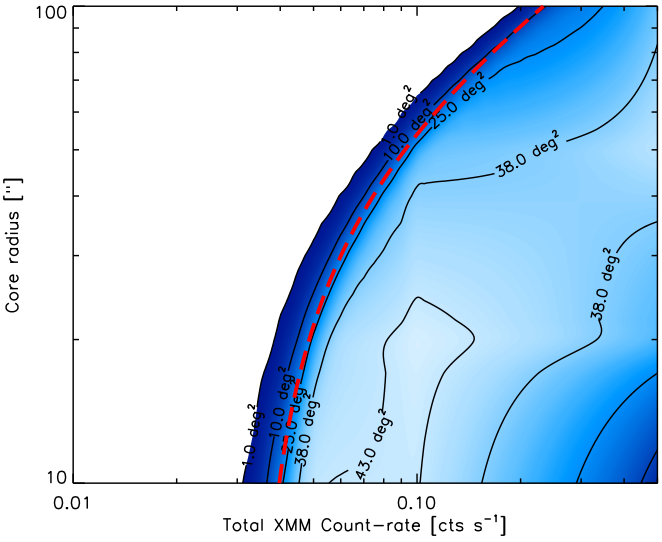

Fig. 9. Sky coverage of the XXL-100-GC sample, displayed as contours of constant sky coverage in the source parameter space - cluster core radius for a β-model with $beta = 2/3$ vs total XMM count rate, summed over the three imaging cameras and integrated to infinite radius. For comparison, the dashed red curve shows the aperture flux cut of $CR_{60} = 0.0332$ cts/s used for the subselection of the bright XXL cluster sample.

6.1. Physical modelling of the cluster population

In all that follows, the cluster mass function is obtained from the Tinker et al. (2008) mass function combined with the high accuracy approximation of the total matter transfer function provided by Eisenstein & Hu (1999), including the effect of BAOs. The cluster mass function is then converted to a temperature function using the average weak lensing $M_{500,\mathrm{WL}}$-$T_{300\ \mathrm{kpc}}$ scaling relation measured in the companion Paper IV, without including the scatter. Finally, we make use of the soft band $L^{\mathrm{XXL}}_{500,MT}$-$T_{300\ \mathrm{kpc}}$ scaling relation obtained in Paper III to model the cluster number per unit volume, n, in X-ray parameter space as:

$$\frac{\mathrm{d}n(L,T,z)}{\mathrm{d}L\,\mathrm{d}T} = \frac{\mathrm{d}n}{\mathrm{d}M\,\mathrm{d}z}\left(\hat{M}\right) \frac{\mathrm{d}\hat{M}(T,z)}{\mathrm{d}T} \mathcal{LN}\left[L\,|\,\hat{L}(T,z), \sigma_{LT}\right], \quad (6)$$

where $\hat{M}(T,z)$ is the average $M_{500,\mathrm{WL}}$-$T_{300\ \mathrm{kpc}}$ scaling relation, $\mathcal{LN}(x|\hat{x},\sigma)$ is a log-normal distribution with Gaussian parameters $\ln(\hat{x})$ and σ, $\hat{L}$ that results from the average $L^{\mathrm{XXL}}_{500,MT}$-$T_{300\ \mathrm{kpc}}$ scaling relation and σ_{LT} is the scatter around this relation. For reference, the parameters of both scaling relations are provided in Table 1. The presence of cool cores with different strengths in a large fraction of the cluster population generates a positive correlation in the scattering of $L^{\mathrm{XXL}}_{500,MT}$ and $T_{300\ \mathrm{kpc}}$ at a given mass, the amount of which remains poorly quantified. Combining the dispersions around both scaling relations without including this correlation would probably overestimate the total scatter. We therefore decided to model only the major contribution to the total dispersion, σ_{LT}.

In order to apply the XXL-100-GC sample selection function, $(L^{\mathrm{XXL}}_{500,MT}, T_{300\ \mathrm{kpc}}, z)$ needs to be converted to an XMM

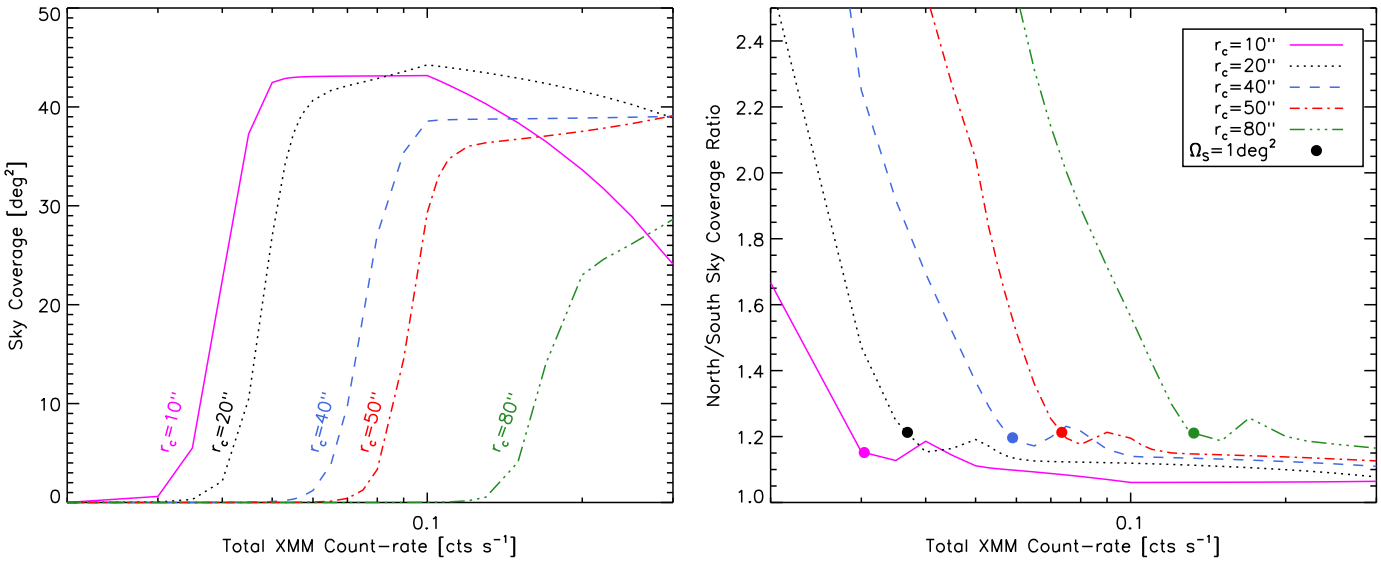

Fig. 10. Sky coverage of the XXL-100-GC sample, displayed as a function of the total XMM count rate (i.e. including the three imaging cameras and integrated to infinite radius). *Left*: Total sky coverage for different cluster core radii. These curves are the slices through the two-parameter selection function displayed in Fig. 9. *Right*: Ratio of sky coverage between the northern and southern fields. For sufficiently large count-rates, the sky coverage of the northern field is consistently 10-15% larger than in the south, while the difference is more pronounced when the total sky coverage falls below 1 deg^2.

Table 1. Reference scaling relations used in the analysis of the [0.5-2] keV luminosity function and cosmological modelling.

Relation	X_0	A_{XT}	B_{XT}	γ	σ_{XT}	Reference
$M_{500,\mathrm{WL}} - T_{300\ \mathrm{kpc}}$	$2 \times 10^{14}\ M_\odot$	1.16	1.67	−1	–	Paper IV
$L^{\mathrm{XXL}}_{500,MT} - T_{300\ \mathrm{kpc}}$	3×10^{43} erg s^{-1}	0.71	2.63	1.64	0.47	Paper III

Notes. For a parameter X, the average scaling with temperature is parametrised as $X/X_0 = A_{XT}\,(T/3keV)^{B_{XT}}\,E(z)^{\gamma_{XT}}$ and the dispersion around the relation follows a log-normal distribution with parameter σ_{XT}.

count rate. For this, we use the on-axis XMM response, an APEC model with metal abundances set to 0.3 of the solar values, and the luminosity distance in the WMAP9 cosmology. In this way, we assume that the difference between $T_{500,MT}$ and $T_{300\ \mathrm{kpc}}$ is negligible and that the result can be identified with the count rate within the projected r_{500}. This is justified because most of the cluster flux originates from within 300 kpc and because we always work in the soft band which minimises the impact of the temperature on the K-correction. As the scatter between mass and $T_{300\ \mathrm{kpc}}$ is larger than with $T_{500,MT}$ owing to the impact of cluster cores, identifying the two values provides us with another justification to neglect the scatter of the $M_{500,\mathrm{WL}}$-$T_{300\ \mathrm{kpc}}$ scaling relation in the modelling of the cluster population.

Finally, a very important assumption is the value of the core radius. Motivated by previous studies of the cluster β-model parameters (e.g. Helsdon & Ponman 2000, Henning et al. 2009, or Alshino et al. 2010), the core radius is assumed to scale linearly with the cluster's physical size as $r_c = x_{500} \times r_{500}$ with $x_{500} = 0.15$ for $\beta = 2/3$. For consistency, the same surface brightness model was also used in Paper III to extrapolate the observed luminosity within 300 kpc to r_{500} and to account for the selection function in the scaling relation fits. In the modelling, it also serves to extrapolate the XMM count-rate within r_{500} to infinity, as required by the definition of the XXL-100-GC sky coverage. We discuss further the impact of the choice of x_{500} in Sect. 7.1.

This model predicts a total of 117 clusters in the fiducial WMAP9 cosmology, slightly more than the actual 100 detections. The significance of this deficit in clusters is less than 1.5 σ accounting for Poisson noise alone, and falls to 1 σ including the additional sample variance arising from cosmic density fluctuations, which we compute following the method of Valageas et al. (2011). The expected redshift distribution is also in reasonable agreement with the observed one (see the left panel of Fig. 11). As a useful cross-check of the modelling assumptions, we directly computed the selection function of the XXL-100-GC sample in terms of mass and redshift for this fiducial cosmology, set of scaling relations, and surface brightness profile. The redshift-dependent mass limit corresponding to a 50% detection probability is shown in Fig. 6. It is consistent with the mass selection as reflected by the distribution of the cluster data points, although it is a bit high at redshift $z > 0.6$. The lack of massive clusters at high redshift combined with the steepness of the mass function suffices to explain the numerous clusters detected just below the 50% completeness limit. We therefore conclude that the number density of the XXL-100-GC sample is fully consistent with the fiducial WMAP9 cosmology.

In comparison, the set of cosmological parameters recently determined by the Planck Collaboration et al. (2015b) from the analysis of the CMB power spectrum measurements of the Planck satellite (Planck Collaboration et al. 2011) significantly overpredicts the density of the XXL-100-GC sample with a to-

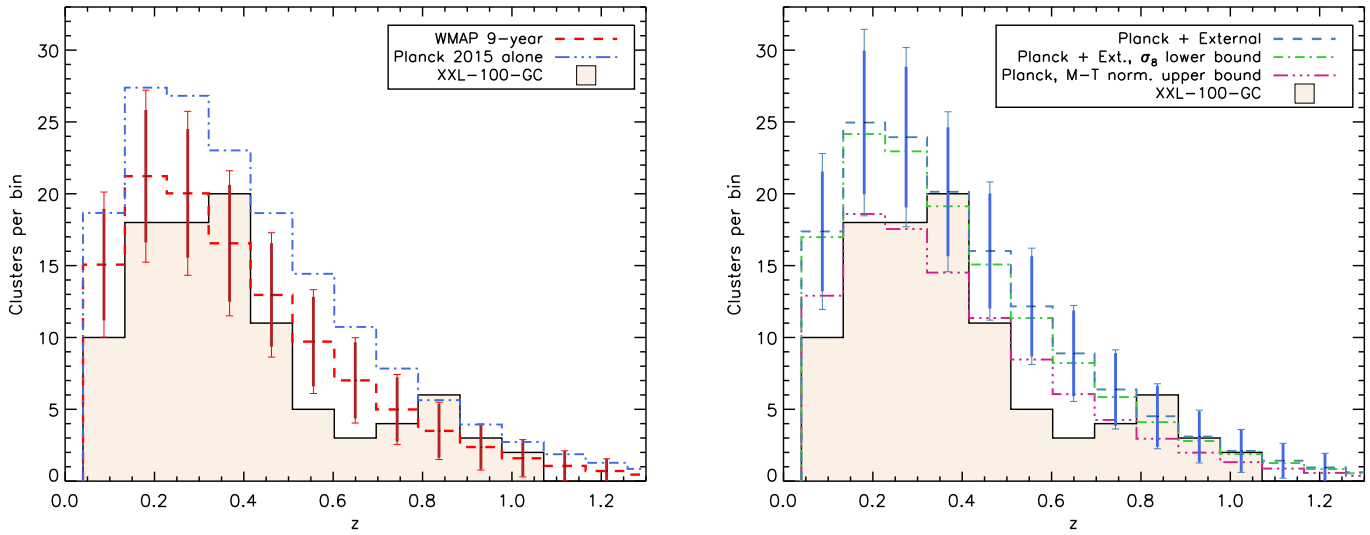

Fig. 11. Redshift distribution of the XXL-100-GC sample (filled histogram) compared with different model expectations. By default, the model predictions are based on the mass and temperature scaling relations of Paper III and Paper IV, and assume a β-model with $\beta = 2/3$ and $x_{500} = 0.15$. *Left*: The fiducial WMAP9 cosmology (red dashed line) compared with the *Planck* 2015 cosmological parameters obtained only from the CMB data (blue dot-dashed). *Right*: Other models derived from Planck Collaboration et al. (2015b). The *Planck*+External set of cosmological parameters includes additional BAO and H0 constraints (blue dashed). The green dot-dashed line is the same, but fixing σ_8 to the 1σ lower bound allowed by the *Planck*+External data set. The purple triple dot-dashed line uses the *Planck*-only parameters, but the normalisation of the $M_{500,WL} - T_{300kpc}$ scaling relation has been increased to its 1σ upper bound. The error bars (shown only for the WMAP9 and *Planck*+External cosmologies) include both the shot noise (thick part) and the cosmic variance.

tal of 165 clusters based on the scaling relations of Paper III and Paper IV[6]. This results in great part from a larger value of $\sigma_8 = 0.831$, but also from the decrease in the Hubble parameter ($H_0 = 67.27\,\mathrm{km\,s^{-1}Mpc^{-1}}$) and the increase in total matter density ($\Omega_m = 0.3156$), which alters both the survey volume (+∼5%) and the mass function (+25−35% depending on mass and redshift). The relative effects of changes in σ_8 or the background geometry can be distinguished by considering the modelled cluster population for a third set of cosmological parameters obtained in Planck Collaboration et al. (2015b) from the combination of their CMB measurement with other cosmological tracers, which we term *Planck*+External cosmology. It has essentially the same geometry as the baseline *Planck* CMB fit and mostly differs in the value of σ_8, which is 0.8159 and therefore comparable to the WMAP9 estimate. Despite the lower σ_8, this model still predicts 143 clusters and outnumbers the observed XXL-100-GC cluster density at all redshifts (see right panel of Fig. 11).

The observed mismatch between the *Planck* CMB results and the late-time tracers of matter fluctuations is well known and was reported by the *Planck* collaboration itself using cluster samples selected with the Sunyaev-Zel'dovich effect (Planck Collaboration et al. 2014; Planck Collaboration et al. 2015c). To investigate the significance of the mismatch with the bright XXL cluster sample, we considered two altered models based on the *Planck* 2015 cosmology (which we also show in the right panel of Fig. 11). In the first, the *Planck*+External set of parameters is assumed with σ_8 fixed to the allowed $1\,\sigma$ lower bound of 0.8073. This only mildly decreases the predicted number of clusters to 136, implying that the uncertainty on the cosmological parameters derived by Planck cannot explain the discrepancy.

[6] These scaling relations were measured assuming the WMAP9 cosmology. Their use is justified here since the distance scales between the two cosmologies only vary by a few percent over the considered redshift range and the fitting procedures do not rely on the normalisation of the mass function, as explained in Appendix C.

In the second model, we stick to the cosmological parameters obtained from the *Planck* CMB dataset alone, but increase the normalisation of the XXL $M_{500,\mathrm{MT}} - T_{300\ \mathrm{kpc}}$ relation of Paper IV to its allowed $1\,\sigma$ upper bound. This alteration in the normalisation at 1 keV also incorporates part of the degeneracy with the slope of the scaling relation, since the median temperature of our sample is closer to 3 keV. Therefore, it serves to approximates a 1σ deviation in the 2D parameter space. This change results in an almost perfect match with 102 predicted clusters. From these considerations, we conclude that the tension between the *Planck* 2015 cosmology and the XXL-100-GC sample cannot yet be established with a strong significance. Further analysis of the XXL cluster population might result in a better agreement.

6.2. Luminosity function

With the prescriptions presented above for the cluster surface brightness profile and scaling relations, we can model the selection effects in the XXL-100-GC sample for population studies.

The most direct statistic widely used to characterise the X-ray cluster population is its luminosity function, which is simply obtained by counting clusters in luminosity bins and correcting for the effective volume probed by the survey. Several methods exist for calculating this correction. In this section, we use the following extimator,

$$\frac{\mathrm{d}n}{\mathrm{d}L}(L) = \frac{\mathrm{d}}{\mathrm{d}L}\left[\frac{N_{>L}}{V_{>L}}\right], \tag{7}$$

which we term the cumulative estimator of the differential luminosity function. Here $N_{>L}$ is the total number of clusters with $L^{\mathrm{XXL}}_{500,MT} > L$ in the redshift slice under consideration, while $V_{>L}$ is the average survey volume for clusters with such luminosities in the same redshift range (defined in the same way as in Eq. (B.7)). In practice, we thus compute the cumulative luminosity function ($N_{>L}/V_{>L}$) and differentiate it numerically. A discussion of other commonly adopted estimators and how they

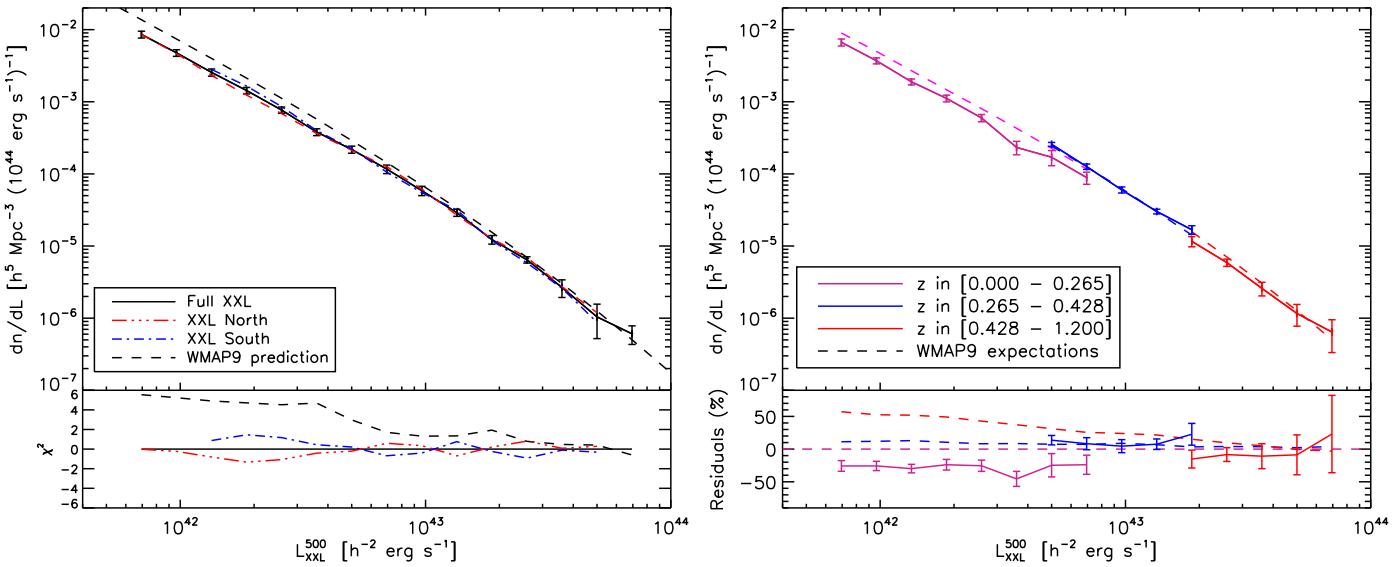

Fig. 12. Differential luminosity function of the XXL-100-GC sample in the WMAP9 cosmology measured with the cumulative estimator defined by Eq. (7). The effective volume correction derives from the XXL-100-GC scaling relations provided in Table 1. The dashed lines show the predictions of the luminosity function in the WMAP9 cosmological model for the same redshift bins as the measurements, and using the same colour code. *Left*: Differential luminosity function averaged over the full redshift range of [0-1.2] covered by the XXL-100-GC sample, and for the northern/southern field separately. The χ^2 plot shows how the deviation of each subfield from the complete analysis compares with the combined error bars. *Right*: Differential luminosity function of the bright XXL cluster sample in three redshift bins. The lower plot shows the residuals with respect to the low-redshift WMAP9 prediction.

compare with the method adopted in this paper is provided in Appendix B. Briefly, the cumulative estimator enables us to estimate the luminosity function for many luminosity values from a reasonably wide luminosity range around each point. This smooths out the shot noise in the estimation and provides tighter error bars at the expense of introducing correlation between the data points.

The errors on the luminosity function were computed from a thousand Monte Carlo simulations and include the effect of shot noise as well as the uncertainties on the measured luminosities and $L^{\rm XXL}_{500,MT} - T_{300\ \rm kpc}$ scaling relation. The number of clusters in each simulation follows a Poisson distribution with a mean of 100. We then generate a bootstrap sample from the cluster catalogue, randomise their luminosities and recompute the luminosity function with a randomised set of scaling relation parameters, derived from the $L^{\rm XXL}_{500,MT} - T_{300\ \rm kpc}$ covariance matrices obtained in Paper III.

The global XXL-100-GC sample luminosity function, averaged over the whole redshift range, is shown in Fig. 12 (left panel), together with expectations for the WMAP9 cosmology obtained by integrating Eq. (6) over temperature and redshift. Assuming the XXL-100-GC set of scaling relations, the agreement between the measurements and the predictions is excellent at intermediate to high luminosities, but we observe a significant deficit of low luminosity clusters in the observed sample ($\sim 4\sigma$, reduced to $2-3\sigma$ when accounting for cosmic variance, which our error models do not include). This is consistent with the 15% higher total cluster counts predicted by the model. The large redshift span and the z versus $L^{\rm XXL}_{500,MT}$ degeneracy that characterises the XXL-100-GC sample however complicates the interpretation of the observed cluster deficit. We observe no hint of deviations between the measurements obtained from the two XXL fields taken separately, although we note that the luminosity function of the northern field reaches fainter luminosities than could be achieved in the south, and that the deficit is more pronounced there.

To proceed further and investigate a possible evolution of the luminosity function, we divided the sample into three mutually exclusive redshift bins ($0 < z < 0.265$, $0.265 < z < 0.428$, and $0.428 < z < 1.2$) containing a similar number of XXL-100-GC clusters (34, 33, and 33, respectively). The resulting luminosity functions are shown in the right panel of Fig. 12. Clearly, the lack of low luminosity clusters apparent in the global luminosity function stems from a slight deficit of low redshift clusters at almost all luminosities. This was already visible, in a more compact way, in the redshift distributions of Fig. 11 where the WMAP9 cosmology predicts more clusters in all bins below $z \sim 0.3$. Within the error bars, we see no hint of evolution between the three redshift bins. This result was first reported by Rosati et al. (1998) for $z \lesssim 0.8$ although, ironically, not in the same cosmology (a flat universe without cosmological constant) and confirmed by a few other studies (see Rosati et al. 2002 for a review). Within the luminosity range probed by the XXL-100-GC sample, this is fully consistent with the predictions of the WMAP9 model, although a strong positive evolution is expected for faint, high redshift clusters, a regime that has not yet been explored by current surveys.

A few studies have also reported a negative evolution of the cluster soft-band luminosity function at high redshift, for instance Mullis et al. 2004 (for clusters at $1.2 < L^{\rm XXL}_{500,MT} < 4.9\times10^{44}$ erg s^{-1} and $0.6 < z < 0.8$) and Koens et al. 2013 (for $0.9 < L^{\rm XXL}_{500,MT} < 12\times10^{44}$ erg s^{-1} and $0.6 < z < 1.1$). We cannot support these findings, but this does not imply any tension since these studies typically involve more luminous clusters than the bulk of the XXL-100-GC population.

Tabulated values of the XXL-100-GC differential and cumulative luminosity functions are given for all considered redshift intervals in Tables 2 and 3.

Table 2. Tabulated values of the XXL-100-GC sample differential luminosity function.

	Full z range		$0.0 < z < 0.265$		$0.265 < z < 0.468$		$0.468 < z < 1.2$	
L_{XXL}^{500}	dn/dL	$\Delta(dn/dL)$	dn/dL	$\Delta(dn/dL)$	dn/dL	$\Delta(dn/dL)$	dn/dL	$\Delta(dn/dL)$
$[10^{42}\,h^{-2}\mathrm{erg\,s^{-1}}]$	[LF unit]†	%	[LF unit]†	%	[LF unit]†	%	[LF unit]†	%
0.69	8.58×10^{-3}	10.8	6.67×10^{-3}	11.1	–	–	–	–
0.97	4.77×10^{-3}	10.6	3.71×10^{-3}	9.6	–	–	–	–
1.34	2.56×10^{-3}	11.4	1.89×10^{-3}	9.3	–	–	–	–
1.86	1.43×10^{-3}	10.3	1.11×10^{-3}	10.6	–	–	–	–
2.59	7.69×10^{-4}	10.0	5.97×10^{-4}	11.5	–	–	–	–
3.60	3.81×10^{-4}	10.8	2.33×10^{-4}	21.1	–	–	–	–
5.00	2.18×10^{-4}	11.2	1.70×10^{-4}	23.7	2.57×10^{-4}	6.3	–	–
6.95	1.17×10^{-4}	13.5	8.88×10^{-5}	19.2	1.26×10^{-4}	8.5	–	–
9.65	5.86×10^{-5}	14.8	–	–	6.01×10^{-5}	9.6	–	–
13.4	2.91×10^{-5}	11.3	–	–	3.02×10^{-5}	7.5	–	–
18.6	1.23×10^{-5}	13.6	–	–	1.68×10^{-5}	13.6	1.16×10^{-5}	16.1
25.9	6.45×10^{-6}	10.1	–	–	–	–	5.90×10^{-6}	11.5
36.0	2.67×10^{-6}	27.5	–	–	–	–	2.59×10^{-6}	21.4
50.0	1.04×10^{-6}	50.0	–	–	–	–	1.16×10^{-6}	33.5
69.5	6.07×10^{-7}	28.8	–	–	–	–	6.42×10^{-7}	48.1

Notes. Because of the luminosity vs redshift degeneracy in the XXL-100-GC sample, only a limited range of luminosities is available for each redshift slice. A graphical display of these values is provided in Fig. 12. $^{(\dagger)}$: all luminosity function values in this table are in units of $[\,h^5\,\mathrm{Mpc}^{-3}\,(10^{44}\,\mathrm{erg\,s^{-1}})^{-1}\,]$.

Table 3. Tabulated values of the XXL-100-GC sample cumulative luminosity function.

	Full z range		$0.0 < z < 0.265$		$0.265 < z < 0.468$		$0.468 < z < 1.2$	
L_{XXL}^{500}	$n(>L)$	$\Delta[n(>L)]$	$n(>L)$	$\Delta[n(>L)]$	$n(>L)$	$\Delta[n(>L)]$	$n(>L)$	$\Delta[n(>L)]$
$[10^{42}\,h^{-2}\mathrm{erg\,s^{-1}}]$	$[h^3\,\mathrm{Mpc}^{-3}]$	%	$[h^3\,\mathrm{Mpc}^{-3}]$	%	$[h^3\,\mathrm{Mpc}^{-3}]$	%	$[h^3\,\mathrm{Mpc}^{-3}]$	%
0.69	6.63×10^{-5}	10.8	5.13×10^{-5}	9.2	–	–	–	–
0.97	4.90×10^{-5}	11.2	3.76×10^{-5}	9.1	–	–	–	–
1.34	3.60×10^{-5}	11.0	2.78×10^{-5}	9.4	–	–	–	–
1.86	2.64×10^{-5}	11.1	2.09×10^{-5}	10.2	–	–	–	–
2.59	1.85×10^{-5}	11.9	1.41×10^{-5}	12.9	–	–	–	–
3.60	1.33×10^{-5}	12.7	1.07×10^{-5}	13.3	–	–	–	–
5.00	9.47×10^{-6}	13.0	8.59×10^{-6}	12.6	1.03×10^{-5}	6.5	–	–
6.95	6.17×10^{-6}	14.9	5.12×10^{-6}	22.3	6.75×10^{-6}	7.4	–	–
9.65	4.14×10^{-6}	12.9	–	–	4.57×10^{-6}	7.3	–	–
13.4	2.44×10^{-6}	15.9	–	–	2.93×10^{-6}	12.3	–	–
18.6	1.57×10^{-6}	16.5	–	–	1.91×10^{-6}	14.7	1.53×10^{-6}	14.9
25.9	9.35×10^{-7}	22.5	–	–	–	–	9.34×10^{-7}	15.0
36.0	4.74×10^{-7}	38.8	–	–	–	–	5.27×10^{-7}	23.9
50.0	3.03×10^{-7}	27.1	–	–	–	–	3.21×10^{-7}	42.2
69.5	1.31×10^{-7}	20.6	–	–	–	–	1.45×10^{-7}	20.8

Notes. Because of the luminosity vs redshift degeneracy in the XXL-100-GC sample, only a limited range of luminosities is available for each redshift slice.

6.3. Constraints from the luminosity distribution

So far, we have assumed that cluster scaling relations are perfectly known from Paper III and Paper IV. In this section, we use the cluster luminosity function to put independent constraints on the parameters of the $L_{500,MT}^{\mathrm{XXL}} - T_{300\ \mathrm{kpc}}$ distribution. This provides a useful consistency check of the cluster luminosity function analysis presented in Sect. 6.2 since we do not use the temperature information, but only the cluster number density[7]. To this purpose, we go back to the raw distribution of the sample in the $(L_{500,MT}^{\mathrm{XXL}}, z)$ plane and compare it with different models using the likelihood function described in Appendix C, a variation over the likelihood derived by Mantz et al. (2010) that also accounts for cosmic variance. For full consistency, we excluded the cluster XLSSC 504 from the fit, as it was also excluded from the $L_{500,MT}^{\mathrm{XXL}} - T_{300\ \mathrm{kpc}}$ analysis of Paper III owing to its suspected AGN contamination and abnormally large temperature. To account for this modification, we included an additional completeness factor of 0.99 in the analysis.

The results are reported in Table 4 for a few different parametrisations of the $L_{500,MT}^{\mathrm{XXL}} - T_{300\ \mathrm{kpc}}$ relation. We first considered a global change in the normalisation of the scaling relation, which yielded slightly lower values than in Paper III. This was to be expected since the fiducial model slightly overpredicts the number of XXL-100-GC sample clusters. Freeing the evolution parameter slightly changes the balance between normali-

[7] The cluster number density was ignored in the analysis of Paper III, as explained in Appendix C

Table 4. Indirect constraints on the $L^{\rm XXL}_{500,MT} - T_{300\ \rm kpc}$ relation parameters obtained by fitting the (L, z) number density.

Free parameters	A_{LT}	B_{LT}	γ_{LT}
Reference	0.71	2.63	1.64
Norm. only	$0.63^{+0.07}_{-0.06}$	2.63	1.64
Norm.+evol	$0.64^{+0.11}_{-0.10}$	2.63	$1.62^{+0.44}_{-0.46}$
Norm.+pow+evol	$0.72^{+0.20}_{-0.15}$	$2.79^{+0.24}_{-0.22}$	$1.26^{+0.67}_{-0.76}$

Notes. The scaling relation parameters are defined in the same way as in Table 1. The error bars include Poisson errors as well as the total cosmic variance predicted for the XXL-100-GC sample using the formalism of Valageas et al. (2011).

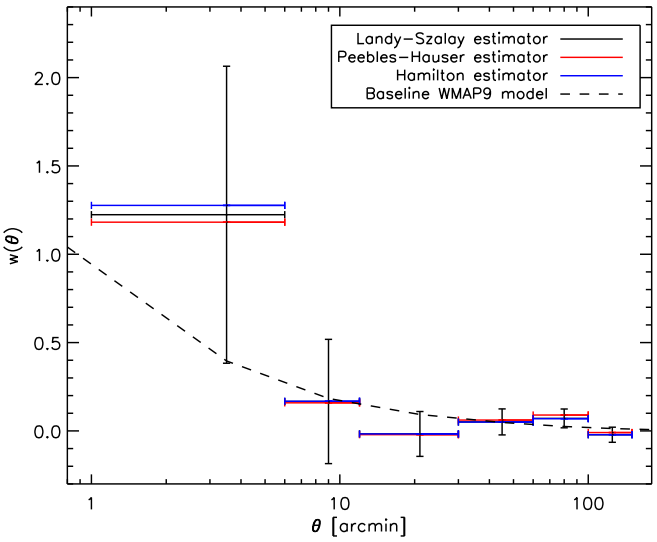

Fig. 13. Angular two-point correlation function of the bright XXL cluster sample. The different levels of correlation come from different estimators. The scatter between these estimators is well within the Poisson uncertainties, shown by the vertical error bars. The dashed line shows the expected correlation in the WMAP9 cosmology with the set of scaling relations obtained in Paper III and Paper IV.

sation and evolution but the deviations are insignificant. Finally, fitting also for the slope of the scaling relation, indicates that the slightly lower density of observed XXL-100-GC sample clusters compared to the fiducial model is better accounted for by a steepening of the scaling relation rather than a change in normalisation.

In all cases, the fitted parameters fall within the statistical errors of the measurements presented in Paper III. Without the temperature information, the data do not allow further constraints on the scatter.

6.4. Spatial distribution

The distribution of the XXL-100-GC clusters over the sky (Fig. 1) shows hints of clustering. To quantify this visual impression, we estimated the two-point angular correlation function (ACF) of the sample. First, we generated random, unclustered catalogs using the 2D selection function maps (see Fig. 7). Each cluster was characterised by its pipeline core radius and its GCA count rate in the 60" aperture and we generated 100 dedicated selection function maps by interpolating over the count rates and core radii used to estimate the sky coverage. Random catalogues with 10000 members were finally obtained by simulating 100 realisations of each cluster's position. From these, we estimated the ACF using the Landy & Szalay (1993), Hamilton (1993) and natural (Peebles & Hauser 1974) estimators. All give closely comparable results and show a positive correlation for scales lower than 6′ (see Fig. 13). This signal is slightly higher than the expectations from the fiducial WMAP9 model (also shown in Fig. 13), but the deviations are compatible within the error bars.

With this small sample and sky projection, the overall significance of this measurement is not high enough yet to derive any useful constraints. To proceed further, we ran a friend-of-friend (FoF) algorithm in the 3D physical space and investigated the presence of large-scale structures among the XXL-100-GC clusters. Previous studies to identify superclusters based on optical cluster samples used linking lengths in the range of 30 to 50 Mpc, for instance 24 h^{-1}Mpc for Einasto et al. (2001) and 20 to 40 h^{-1}Mpc (redshift dependent) for Chow-Martínez et al. (2014). We therefore opted for a linking length of 35 Mpc. This value matches the average linking length used by Chon et al. (2013), who considered several percolation thresholds applied to the REFLEX-II X-ray cluster sample (Böhringer et al. 2014).

To qualify as a superstructure, a FoF detection had to contain at least three connected XXL-100-GC clusters, and among these at least one pair had to have a separation of less than 10 Mpc, which corresponds to ~ 10 times the virial radius of a cluster of mass $M_{500} = 2 \times 10^{14}$ at redshift $z = 0.3$. This second criterion ensures that the detected superclusters are gravitationally bound.

With this procedure, we identified five structures. We summarise here their main properties:

- XLSSC-a is a very nearby ($z \sim 0.05$) association of four groups spread over the whole XXL-North field. All four groups belonging to the XXL-100-GC sample – XLSSC 011, XLSSC 052, XLSSC 054, and XLSSC 062 – have luminosities in the range $1 - 3 \times 10^{42}$ erg s^{-1}.
- XLSSC-b shows two subcomponents located at a redshift of $z \sim 0.14$. The eastern part consists of four XXL-100-GC clusters (including the merger XLSSC 050), while the western part is concentrated around one of the three Abell clusters located in the northern XXL field (XLSSC 060, also known as Abell 329).
- XLSSC-c is located at $z = 0.17$ and is the only superstructure that we found in the southern field. Centred on the double system XLSSC 535/536 (see Appendix A for more details), it consists of six clusters, all from the XXL-100-GC sample.
- XLSSC-d consists of four XXL-100-GC clusters plus three other XXL C1+2 clusters located at redshift $z = 0.29$.
- XLSSC-e is located at $z = 0.43$ and consists of six clusters, three of which belong to the XXL-100-GC sample. This structure is exceptionally compact over the sky; all the clusters reside in the same XMM pointing. It is. however, much more elongated along the line of sight. This structure is the subject of Pompei et al. (2016, hereafter Paper VII).

Their characteristics are provided in Table 5 and the 3D configuration of each structure is shown in Fig. 14. Interestingly, they can explain the previous measurement of the ACF very well. Indeed, for separations lower than 12′, structures XLSSC-c, XLSSC-d and XLSSC-e account for almost all the excess of pairs above the random distribution.

In the process, we also found two nearby pairs of clusters with distances of less than 10 Mpc. They consist of (XLSSC 524, XLSSC 519) at redshift $z = 0.270$ and (XLSSC 103, XLSSC 055) at $z = 0.232$.

Table 5. Properties of the five XXL-100-GC superstructures.

Name	RA	Dec	z	N_{cl}	$M_{\rm tot,MT}$	XLSSC Members
-	[deg]	[deg]	-	-	$10^{14}\,M_\odot$	-
XLSSC-a	36.55	-4.06	0.05	4	3.2	011, 052, 054, 062
XLSSC-b	35.39	-4.70	0.14	7	10.3	041, 050, 060, 087, 090, 095, 112
XLSSC-c	350.67	-54.48	0.17	6	6.3	514, 518, 520, 530, 535, 536
XLSSC-d	37.22	-5.05	0.29	4	8.5	022, 027, 088, 104
XLSSC-e	32.87	-6.20	0.43	3	11.9	083, 084, 085

Notes. RA,Dec: WCS coordinates are in the J2000 system; these were computed from the mean of the cluster member positions, except for XLSSC-e where the position of the central massive cluster XLSSC 085 was used. N_{cl}: number of XXL-100-GC clusters pertaining to the structure. $M_{\rm tot,MT}$: sum of the $M_{500,\rm MT}$ masses of all members.

7. Summary and discussion

We have defined and presented the XXL-100-GC galaxy cluster sample, a complete subsample of the full XXL extended source catalogues, which consists of 100 clusters above a flux cut of 3×10^{-14} erg s^{-1}cm^{-2} in a 60″ aperture. The selection function of the sample was carefully estimated, for β-model clusters, including the initial pipeline selection, the additional flux cut, as well as the layout and depth of the XXL observations. We have obtained spectroscopic redshifts for 97 of the clusters and reliable photometric redshifts for the 3 remaining ones. Based on the mass and temperature scaling relations self-consistently measured from the same sample in Paper III and Paper IV, we compared the redshift distribution of the sample with model predictions and found that the XXL cluster population is better reproduced by low σ_8 models such as the WMAP9 cosmology than models with higher values of σ_8 like the one obtained recently from the *Planck* satellite. We then studied the luminosity function of the sample and again obtained results that are overall consistent with the WMAP9 model, the only discrepancy being a lack of low luminosity, low redshift clusters. The luminosity function shows no sign of evolution at any redshift, confirming some earlier findings but contrasting with claims of a negative evolution at high redshift for more luminous clusters (Mullis et al. 2004; Koens et al. 2013). An attempt to fit the $L^{\rm XXL}_{500,MT} - T_{300\ \rm kpc}$ scaling relations indirectly to the luminosity and redshift distribution of the sample proved consistent with the results of Paper III, which were based on the measured cluster temperatures. Finally, we reported a significant clustering of sources on scales smaller than 6′, which we entirely resolved into five large-scale superclusters identified using FoF techniques.

In this section, we examine the impact of the main assumptions on the derived results and consider the implications of the present work for the next steps of the XXL project.

7.1. The cluster number density

The deficit of clusters at low luminosity compared to the WMAP9 expectations and the absence of evolution in the cluster luminosity function are certainly the most significant results obtained by the analysis of the XXL-100-GC sample number density presented in Sect. 6. They all rely on the central assumption that the cluster emission profile is represented well by a simple β-model with fixed $\beta = 2/3$ and $x_{500} = r_c/r_{500}$ of 0.15. To check the robustness of these findings, we reproduced the whole analysis for different values of x_{500}. Luminosities in $r_{500,\rm MT}$ were re-evaluated from the measurements in 300 kpc apertures based on the new β-model profiles. Then, the effective volume probed by the survey was updated with the corresponding selection functions and the altered $L^{\rm XXL}_{500,MT} - T_{300\ \rm kpc}$ scaling relations provided in Paper III. The resulting XXL-100-GC luminosity functions are shown in Fig. 15 for $x_{500} = 0.1$ and 0.2, which provide conservative boundaries for this parameter. The change is greatest for luminosities below $6 \times 10^{43}\,{\rm h}^{-2}{\rm erg\,s}^{-1}$, but never exceeds $\sim 1\sigma$. Consequently, although the uncertainty on x_{500} would make a significant contribution to the error budget, it does not yield changes large enough to affect our conclusions.

To further check that the observed lack of clusters is real, we also compared the XXL-100-GC measurements at low redshift ($z < 0.4$) with the best fit luminosity function obtained by the REFLEX-II collaboration (Böhringer et al. 2014), the largest complete sample of low redshift X-ray clusters available to date. This was rescaled by a global factor of 0.59 to account for different spectral bands[8]. As is evident from Fig. 16, the REFLEX-II luminosity function is significantly flatter than both the XXL-100-GC measurements and the WMAP9 prediction. More precisely, in the XXL-100-GC sample, we observe 30% fewer bright objects and 40% more low luminosity clusters. Such deviations are well above the uncertainties arising from the assumed spectal band correction, and also larger than the expected ∼15% fluctuations from Poisson and cosmic variance over the whole sample. As the two samples are not drawn from surveys of the same depth, the average redshifts probed by any given luminosity bin differ. However, the absence of redshift evolution in the XXL-100-GC luminosity function analysis rules out this possible explanation. More likely, most of the discrepancy originates in the methods used to estimate the cluster luminosities. Indeed, the r_{500} apertures used by the REFLEX-II collaboration are not based on the same set of scaling relations and rely on the cluster luminosities through an iterative procedure. Then, the initial extraction radius for the luminosity estimates and the recipe for the aperture correction differ. In addition, the K-correction is applied in a different way and does not account for the scatter in the $L_X - T$ scaling relation. Despite these differences, it is possible that some of the mismatch could come from the properties of the XXL fields themselves. The two fields follow the optical footprint of optical surveys that purposely avoided the presence of very local bright clusters. More importantly, on the low-luminosity end, most of the information in the XXL-100-GC sample comes from the northern field, as a result of the presence of the superstructure XLSSC-a. Given the density of this structure, which covers the whole northern field, it is likely that the XXL-100-GC luminosity function estimates lie on the upper end of the real space density of clusters in this luminosity range, which would bring the REFLEX-II measure-

[8] For temperatures between 0.5 and 5 keV, and redshifts between 0 and 0.4, the K-correction between the [0.5 − 2] and [0.1 − 2.4] keV bands mostly shows variations lower than 5%.

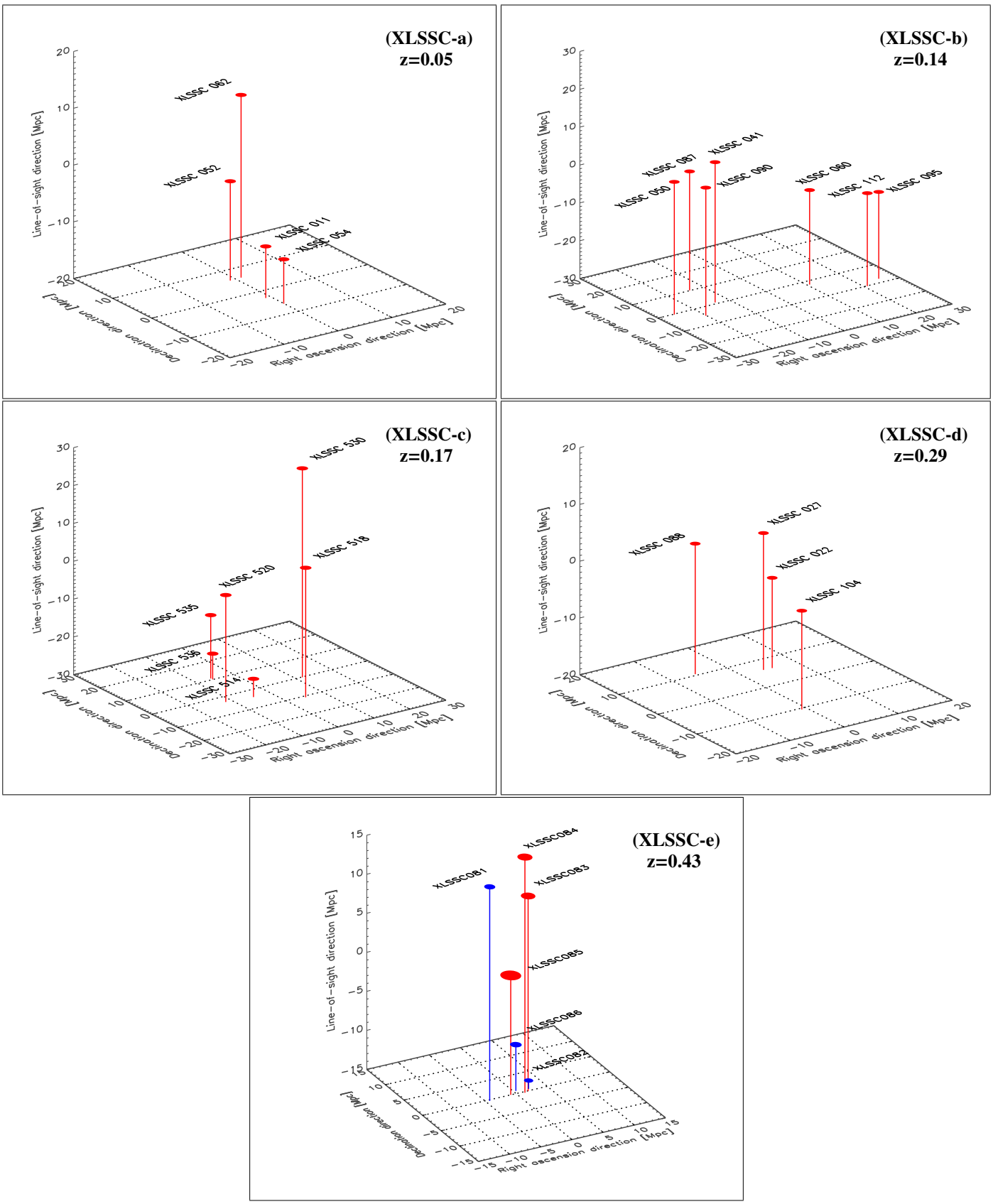

Fig. 14. Three-dimensional configuration of five superstructures identified in the bright XXL cluster sample. *XLSSC-a*: located in the northern field with an average redshift of $z \sim 0.05$. *XLSSC-b*: a double structure in the northern field at $z \sim 0.14$. The western component is centred on XLSSC 060 (also known as Abell 329). *XLSSC-c*: located in the southern field at $z \sim 0.17$. It is centred on the cluster Abell 4005, which we resolve into two subcomponents (XLSSC 535 and 536). *XLSSC-d*: located in the northern field at $z \sim 0.29$. The central pair of clusters has already been identified in the XMM-LSS in Pacaud et al. (2007). *XLSSC-e*: This $z = 0.43$ supercluster in the northern field is studied in depth in Paper VII. Clusters published in Paper VII that do not pertain to the XXL-100-GC sample are in blue. The symbol size reflects the cluster masses inferred in Paper VII.

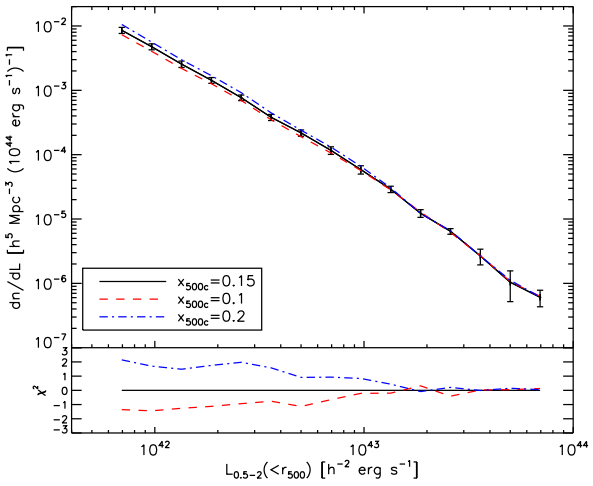

Fig. 15. Impact of different choices of $x_{500} = r_c/r_{500}$ on the XXL-100-GC luminosity function.

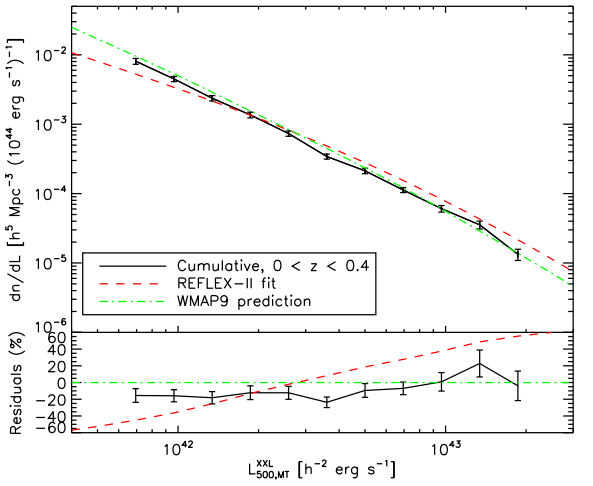

Fig. 16. Differential luminosity funcion averaged in the redshift range [0-0.4], computed in the same way as for Fig. 12, in comparison with measurements from RELEX-II in the same redshift range and predictions for the WMAP9 model. The residual plot shows the fractional deviation with respect to the model predictions.

ments into better agreement, but would make the deviation from the WMAP9 model even larger.

From these considerations, we conclude that the lack of observed XXL-100-GC sample clusters at low luminosity is probably genuine and reflects the fact that the WMAP9 and scaling relation model used in this paper only provides a first-order description of the cluster density in the XXL fields.

In the 11deg^2 XMM-LSS field, Clerc et al. (2014) also observed a deficit of clusters in the $0.5 < z < 0.7$ range. There is no sign of such a deficit in the rest of the XXL area, so the earlier results should be ascribed to a cosmic void.

7.2. Large-scale structures

Historically, the searches for superstructures in the distribution of galaxy clusters started with the first Abell catalogues (see e.g. Batuski & Burns 1985 and Kalinkov & Kuneva 1995 for the largest samples). Since then, superclusters of lower total mass have been identified from comprehensive spectroscopic surveys such as the 2dF galaxy redshift survey (Einasto et al. 2007) or the Sloan Digital Sky Survey (Einasto et al. 2014), but remained limited to the local universe ($z \lesssim 0.1$). Recently, Chon et al. (2013) extended the volume used for such studies to $z \lesssim 0.3$ and presented the first supercluster catalogue identified from a complete X-ray selected cluster sample. This new selection method has the advantage of relying only on galaxy structures that show clear evidence of a deep potential well. Although a few isolated very high redshift superclusters are known (e.g. Gal & Lubin 2004), our work is the first attempt to systematically unveil superstructures up to $z \sim 0.5$ in a homogeneous X-ray sample. In addition, the detected structures do not correspond to the traditional picture of superclusters as very massive systems ($\sim 10^{15} - 10^{16}$ M$_\odot$) currently starting to collapse, but rather exhibit masses similar to low redshift massive clusters. These clusters can tell us about the large-scale structure of the Universe, but they can also provide a unique opportunity to witness the formation process of current galaxy clusters and understand the origin of their observational properties. With an XXL sample that is four times larger, we shall therefore be able to build the first representative sample of more than 10 clusters in the early days of their formation and use the associated XXL multiwavelength data set to study the galaxy population in these systems as well as their ICM properties.

The 1.5σ evidence of correlation on scales of less than 6 arcmin is encouraging for the XXL goal of measuring the 3D correlation function. With more than 450 clusters expected for the full sample, the relative uncertainty on the angular correlation function will decrease by a factor of ~ 4, enabling a significant measurement in a few angular bins. As shown in Valageas et al. (2011), the signal-to-noise ratio for the 3D correlation function averaged over the survey volume will be even higher. Their figure 12 demonstrates that a significant detection of positive correlation should already be obtained for about six bins between 5 and 30 h^{-1}Mpc for a 50deg^2 survey with a single mass limits of 10^{14} M$_\odot$, a selection that is similar to the XXL-100-GC sample in terms of number density and average mass. However, random catalogs for the 3D cluster distribution cannot be easily obtained in a model-independent way as we did for the projected sky distribution. They depend very much on the choice of underlying cosmology and scaling relations. We therefore defer the measurement of the correlation in 3D to a later work where the use of the 3D correlation for cosmological constraints will be explored in detail.

7.3. Cosmological leverage of the bright XXL cluster sample

Obtaining competitive constraints on the dark energy equation of state is a major science goal of the XXL Survey. To assess the constraining power already achieved with the XXL-100-GC sample, we ran an illustrative cosmological analysis based on the luminosity and redshift distribution of the sample, using the formalism described in Sect. 6.3 and Appendix C. This is very similar to the analysis performed in Mantz et al. (2008), except that we use an unbinned likelihood that includes cosmic variance.

As a first attempt, we fix all scaling relation parameters to the fiducial XXL values and fitted σ_8 while fixing all other cosmological parameters to their fiducial values. This resulted in a lower value than the WMAP9 model with $\sigma_8 = 0.807 \pm 0.018$, as expected from the observed deficit of low redshift clusters. Even with this perfect mass calibration, the achieved uncertainties are of nearly the same magnitude as the mismatch between the values of σ_8 obtained by Planck and those determined by WMAP9 or from late-time tracers of matter fluctuations. Therefore, the XXL-100-GC sample alone is not large enough to pre-

cisely investigate this issue. We also allowed the parameters of the $L^{\rm XXL}_{500,MT} - T_{300\ \rm kpc}$ scaling relation to be fitted, including priors according to the measurements of Paper III. Owing to the XXL likelihood model, these measurements are essentially independent of the normalisation of the mass function (here governed by σ_8) and mostly result from the temperature information (which we neglect), so they can be considered as independent constraints. This second fit yields $\sigma_8 = 0.814^{+0.037}_{-0.034}$ and implies that the ability to constrain cosmology with XXL is currently limited by the cluster mass calibration, even with the XXL-100-GC subsample. Finally, fitting also for Ω_m, we observe a strong degeneracy and the marginalised error on σ_8 becomes $\Delta\sigma_8 \sim 0.05$ even when the scaling relation parameters are held fixed. This does not come as a surprise. Even with the final XXL cluster sample and using the cluster 3D correlation function, which together improve the constraining power of the survey by a factor ~ 4, it was already noted in Pierre et al. (2011) that the combination with other cosmological probes (e.g. CMB measurements from *Planck*) would be necessary to break the cosmological degeneracy and isolate constraints on the evolution of dark energy.

As already mentioned, the assumed model of the cluster surface brightness profile (as summarised by the x_{500} parameter) can also have a significant impact on the above results. The modified models with x_{500}=0.1 and 0.2 discussed in Sect. 7.1 respectively predict a total of 134 and 100 clusters, i.e. changes comparable with the Poisson noise standard deviation. Repeating the σ_8 analysis for these models, we observe that the statistical errors remain unchanged, but the best fit value varies (by, respectively, +0.003 and -0.010). The shift in σ_8 is smaller than the most optimistic error bars obtained in the previous paragraph (i.e. neglecting both uncertainties on scaling relation and cosmological degeneracies); therefore, a reasonable change in x_{500} has little impact on the cosmological constraints achievable from the XXL-100-GC sample. However, this additional uncertainty will become very important for the modelling of the complete XXL sample. In a later work (Démoclès et al., in prep.) we will self-consistently address the determination of x_{500} using the XXL-100-GC sample to reduce this source of modelling uncertainty. Another concern would be the existence of a subpopulation of clusters with centrally peaked surface brightness profiles due to either cool-cores or central AGN contamination, since such clusters might fail to pass the pipeline C1+2 extension criteria. To evaluate the possible impact of such a subpopulation of clusters on the XXL-100-GC sample, we adopted a data-oriented method. First, we inspected visually a random subsample of 100 XXL point-like sources with a measured pipeline count rate above the XXL-100-GC aperture flux limit. None of those sources was a likely cluster candidate. Assuming a binomial likelihood, it implies a 1σ upper limit of 1.1% on the proportion of genuine clusters among the sources above the aperture flux classified as point-like by the pipeline. Since the XXL AGN sample in good pointings contains fewer than 1000 such sources, we estimate an upper limit of 10 missing clusters due to centrally concentrated profiles. This number is again lower than the Poisson noise. In addition, we screened all the soft band point-like sources that were detected as extended in the hard [2-10] keV band. This enabled us to recover two bright and very compact low redshift clusters (XLSSC 118 and XLSSC 552) whose properties are detailed in Table D.2 and Appendix A. Although they show traces of point-source contamination, they seem to be genuinely extended but very centrally peaked systems. As the impact of cluster morphology on the XXL pipeline selection function does not seem to strongly affect the results of the present work, we defer a more detailed analysis to forthcoming XXL papers.

8. Conclusions

In this work, we introduced the bright XXL cluster sample, a subsample of the hundred brightest XXL clusters detected in the available 46.6 deg^2. The source selection process consists of a 3×10^{-14} erg s^{-1}cm^{-2} aperture flux cut within a $1'$ radius in addition to the initial XXL pipeline. All but four sources were confirmed with optical spectroscopy and the selection function of the sample was carefully modelled. We were able to determine well-constrained X-ray temperatures, and luminosities for most of them and even weak lensing masses for a subsample of 38 clusters. This allowed for a self consistent analysis of the cluster number density (in this article) together with the cluster scaling relations (in Paper III and Paper IV).

We studied the luminosity function of the sample and concluded that it does not evolve over the considered redshift range. The observed luminosity and redshift distributions match low σ_8 models more closely than the currently favoured *Planck* cosmology. However, the alternate WMAP9 model is not perfect either and overpredicts the amount of faint clusters. We detected a positive angular correlation between the XXL-100-GC clusters, which we were entirely able to resolve into five new superclusters detected in the XXL field. These structures are likely progenitors of local massive clusters and will shed light on a new phase of the build-up of galaxy clusters across cosmic times.

Basic attempts to assess the cosmological leverage of the sample revealed that, even with the current subsample, the error budget is already dominated by uncertainties in the cluster mass calibration, which therefore will be one of the priorities of the XXL cluster science program over the next few years. The situation will improve significantly in the near future with the deeper weak-lensing observations currently being performed over the whole XXL field (see Paper I for details), the introduction of additional cluster mass indicators, and further cluster follow-up studies.

Extrapolating from the observed XXL-100-GC cluster population, we expect the whole XXL X-ray analysis to yield some 450 cluster detections, which is consistent with the current list of XXL cluster candidates, but significantly less than the initial predictions from Pierre et al. (2011). Cluster count predictions in this forecast article were done on the basis of ad hoc scaling relations and a very rough approximation for the cluster shape (β-models with a constant core radius of 180 kpc). A thorough analysis of the cluster density will be given when the full cluster catalogue is published. In this future paper, we shall explore the selection function in greater detail and consider the effect of cluster morphology, cool cores, baryon physics, and AGN contamination by means of high-resolution hydrodynamical simulations and semi-analytic models (cf. Paper I).

The detailed properties of the XXL-100-GC sample will be distributed through the dedicated XXL cluster database[9], together with the seven complementary clusters detected in contaminated pointings but bright enough to exceed the XXL-100-GC aperture flux cut. A master XXL-100-GC cluster catalogue will also be available in electronic form in the XXL Master Catalogue Database in Milan[10]. Public access to both databases will occur after the paper is accepted.

[9] http://xmm-lss.in2p3.fr:8080/xxldb/
[10] http://cosmosdb.iasf-milano.inaf.it/XXL/

Acknowledgements. XXL is an international project based around an XMM Very Large Programme surveying two 25 deg^{2}extragalactic fields at a depth of $\sim 5 \times 10^{-15}$ erg s^{-1} cm^{-2}in [0.5-2] keV. The XXL website is `http://irfu.cea.fr/xxl`. Multiband information and spectroscopic follow-up of the X-ray sources are obtained through a number of survey programmes, summarised at `http://xxlmultiwave.pbworks.com/`.
This research has made use of the NASA/IPAC Extragalactic Database (NED) which is operated by the Jet Propulsion Laboratory, California Institute of Technology, under contract with the National Aeronautics and Space Administration. This research has made use of Aladin sky atlas and SIMBAD database, both developed at CDS, Strasbourg Observatory, France. In particular, we would like to thank Thomas Boch for his help with Aladin Lite.
FP acknowledges support from the BMWi/DLR grant 50 OR 1117, the DFG grant RE 1462-6 and the DfG Transregio Programme TR33. TR acknowledges support from the DFG Heisenberg grant RE 1462-5. The Saclay group acknowledges long-term support by the Centre National d'Etudes Spatiales (CNES). BJM, PAG and MB acknowledge support from STFC grants ST/J001414/1 and ST/M000907/1. The Dark Cosmology Centre is funded by the Danish National Research Foundation.
The XXL team would also like to thank the VLT support astronomers C. Hummel and N. Neumayer for their dedicated help in the implementation of the XXL ESO Large Program and with the data reduction.

Appendix A: Notes on individual clusters

- XLSSC 041: at redshift $z = 0.14$, overlaps with a fainter background galaxy cluster, XLSSC 045, at $z = 0.556$ (Adami et al. 2011).
- XLSSC 050: at redshift $z = 0.14$, is a very elliptical cluster showing clear signs of merging activity. In particular, all of its bright galaxy members are located on opposite sides of the ellipsoid, suggesting a significant offset between the gas and collisionless material.
- XLSSC 052: a large fraction of the X-ray emission overlaps a bright saturated star, BD-03 381 from the Tycho catalogs (Hog et al. 1998).
- XLSSC 057: is the X-ray counterpart of Abell 334 (Abell et al. 1989). The offset between the optical and X-ray detection is 2.9′.
- XLSSC 060: is the X-ray counterpart of Abell 329 (Abell et al. 1989). The offset between the optical and X-ray detection is 0.7′. This cluster is also part of the *Planck* Sunyaev-Zel'dovich cluster catalogue (Planck Collaboration et al. 2015a) as PSZ2 G167.98-59.95. The infered XXL $M_{500,\mathrm{MT}}$ falls within 2% of that reported by the Planck team.
- XLSSC 062: the X-ray emission is possibly dominated by three bright central galaxies.
- XLSSC 083/XLSSC 084: part of the supercluster studied in Paper VII. Their X-ray emission significantly overlap.
- XLSSC 085: the cluster is surrounded by two X-ray AGNs. Although they are correctly identified and masked by the pipeline, the cluster remains an outlier in the $M_{500,\mathrm{WL}} - T_{300\ \mathrm{kpc}}$ scaling relation presented in Paper IV, possibly indicating a residual contamination.
- XLSSC 089: extremely compact and rich system at $z = 0.609$ where most of the X-ray emission and all of the seven spectroscopically confirmed members are found within a 30″ aperture.
- XLSSC 090: fossil group at $z = 0.141$.
- XLSSC 091: is the X-ray counterpart of Abell 362 (Abell et al. 1989). The offset between the optical and X-ray detection is 2.0′. This cluster is also part of the *Planck* Sunyaev-Zel'dovich cluster catalogue (Planck Collaboration et al. 2015a) as PSZ2 G174.40-57.33. The infered XXL $M_{500,\mathrm{MT}}$ falls within 14% of the value reported by the Planck team.
- XLSSC 094: the X-ray emission is probably contaminated by a background AGN ($z = 1.11$) located precisely at the peak of the X-ray emission.
- XLSSC 096: the main galaxy cluster at $z = 0.520$ is superimposed on another redshift overdensity at $z = 0.203$. The bright galaxies at $z = 0.520$ follow the central X-ray overdensity, while the low redshift system is much more sparse.
- XLSSC 104: a secondary peak is apparent in the X-ray emission and probably indicative of some AGN contamination. The cluster is an outlier in the $M_{500,\mathrm{WL}} - T_{300\ \mathrm{kpc}}$ scaling relation presented in Paper IV.
- XLSSC 110: at $z = 0.445$ show strong lensing arcs around the probable brightest cluster galaxy.
- XLSSC 113: nearby group at $z = 0.050$ with signs of emission from individual member galaxies.
- XLSSC 118: bright and surprisingly compact ($x_{500} \sim 0.02$) cluster at $z = 0.140$, classified as a point source by the XXL detection pipeline in the [0.5-2] keV band but recovered as extended in the [2-10] keV band. The surface brightness shows traces of point-source contamination.
- XLSSC 504: one of the faintest clusters in the XXL-100-GC sample. The emission is very compact and peaked with signs of extension to the north-west, suggesting significant contamination by a central AGN. This is confirmd by the presence of a bright flat-spectrum radio source detected in the PARKES-MIT-NRAO (Gregory et al. 1994) and SPT (Mocanu et al. 2013) surveys. The temperature measured in Paper III without excluding the AGN is very high but the faint signal does not allow a better analysis. Consequently, this cluster is not included in the scaling relation and cosmology fits presented in this paper and in Paper III (which we account for with an additional incompleteness factor of 0.99).
- XLSSC 513: This cluster was detected by the SPT collaboration (Bleem et al. 2015) as SPT-CL J2316-5453. The inferred XXL $M_{500,\mathrm{MT}}$ falls within 19% of the value reported by the SPT team.
- XLSSC 514/XLSSC 515: their separation on the sky is less than 2′. Two clear redshift overdensities are visible at $z = 0.101$ and 0.169 , associated with two distinct peaks in the X-ray emission. However, the X-ray analysis might be affected by the superposition.
- XLSSC 516: was assigned a photometric redshift of $z = 0.87$. The X-ray emission, although surrounded by two AGNs, seems genuinely extended. Despite a first attempt to observe it with VLT/FORS2, the cluster has not yet been confirmed. However, VLT/HAWK-I near infrared imaging suggests a highly compact cluster, not visible in the optical images. The photometric redshift is therefore probably underestimated.
- XLSSC 523: is the X-ray counterpart of Abell S1115 (Abell et al. 1989). The offset between the optical and X-ray detection is 1.5′.
- XLSSC 526: is the X-ray counterpart of Abell S1112 (Abell et al. 1989). The offset between the optical and X-ray detection is 1.3′.
- XLSSC 535/XLSSC 536: are the X-ray counterparts of Abell 4005 (Abell et al. 1989), with the optical centre located right in between the two X-ray detections. The two clusters are aligned in the north-south direction which calls for a redefinition of Abell 4005 as Abell 4005N (XLSSC 535) and Abell 4005S (XLSSC 536). Taken at face value, the coordinates and redshift of the two subcomponents indicate a separation of ~ 9 Mpc. However, their angular separation only corresponds to 700 kpc and most of the distance could be accounted for by a Doppler shift of ~ 700 km s^{-1}, a plausible value for two clusters heading toward each other. Therefore we cannot exclude that the two clusters are already in an

early merging phase. This pair of clusters forms the centre of a larger superstructure, structure 2, described in Sect. 6.4.
- XLSSC 539: shows two reshift structures at $z = 0.169$ (3 concordant redshift) and $z = 0.182$ (2 redshifts). In the absence of a better criterion, we opted for the richest structure.
- XLSSC 541: is the X-ray counterpart of Abell 4027 (Abell et al. 1989). The offset between the optical and X-ray detection is 0.5′.
- XLSSC 542: is part of the Planck Sunyaev-Zel'dovich cluster catalogue ß(Planck Collaboration et al. 2015a) as PSZ2 G325.99-59.48. The inferred XXL $M_{500,\mathrm{MT}}$ falls within 10% of the value reported by the Planck team. The cluster was also detected by the SPT collaboration (Bleem et al. 2015) as SPT-CL J2332-5358. Their mass estimate for the cluster deviates by only 16%.
- XLSSC 549: was assigned a redshift of $z = 0.808$ based on three, well-centered, concordant redshifts. However there seems to be a second structure along the same line of sight at $z = 0.568$ with two redshifts.
- XLSSC 552: is a bright and surprisingly compact ($x_{500} \sim 0.03$) cluster at $z = 0.152$, classified as a point source by the detection pipeline in the [0.5-2] keV band but recovered as extended in the [2-10] keV band. Possible but relatively small point-source contamination.

Appendix B: Comparison of luminosity function estimators

The luminosity function is most often measured (e.g. Mullis et al. 2004 or Böhringer et al. 2014) by dividing the cluster sample into luminosity bins of width ΔL_i and using the estimator

$$\frac{\mathrm{d}n}{\mathrm{d}L}\left(< L_i >\right) = \frac{1}{\Delta L_i}\sum_{j=0}^{N_i}\frac{1}{V_{eff}(L_j)}, \tag{B.1}$$

where $< L_i >$ is the centre of luminosity bin i, the summation runs over the N_i detected clusters in that bin, and V_{eff} is the luminosity dependent effective volume from which each cluster was selected (accounting for the sky coverage). In this appendix, we refer to this estimator as the 'point correction' method. It is easy to implement and has the advantage that the error bars of the different bins are uncorrelated, which renders subsequent statistical analyses easier.

To compute the effective volume, V_{eff}, the survey sky coverage first needs to be recast as a function of the cluster luminosity and redshift, namely

$$\Omega_S\left(L,T,z\right) = \Omega_S\left(CR_\infty\left[L,T,z\right], x_{500}r_{500}\left[\hat{M}(T,z)\right]\right) \tag{B.2}$$

and

$$\Omega_S\left(L,z\right) = \frac{\int_T \frac{\mathrm{d}n(L,T,z)}{\mathrm{d}L\,\mathrm{d}T}\Omega_S\left(L,T,z\right)\mathrm{d}T}{\int_T \frac{\mathrm{d}n(L,T,z)}{\mathrm{d}L\,\mathrm{d}T}\mathrm{d}T}, \tag{B.3}$$

where $\hat{M}(T,z)$ is the average mass-temperature scaling relation and $\mathrm{d}n/\mathrm{d}L\mathrm{d}T$ is the volumic density of clusters defined in Eq. (6). This accounts for the distribution in M_{500} and T at given $L^{\mathrm{XXL}}_{500,MT}$ and z in the assumed cosmological model to compute an average sky coverage. We note that the mass function in the chosen cosmology, as well as cluster scaling relations, implicitely enters the calculation of the sky coverage. This is necessary since the detection efficiency depends on the mass (through its link to the core radius) and temperature (to compute the spectral K-correction).

The effective survey volume for given $L^{\mathrm{XXL}}_{500,MT}$ and z is then readily obtained as:

$$V_{eff}\left(L\right) = \int_z \frac{\mathrm{d}^2V}{\mathrm{d}\Omega\,\mathrm{d}z}\Omega_S\left(L,z\right)dz. \tag{B.4}$$

For sparsely populated samples, where the density of points is too low to properly weight the effective volume between the different luminosities within a bin, the correction for the sky coverage can become noisy. In this case one can directly compute the average sky coverage within the luminosity bin from the same cosmological model that was used to determine the luminosity dependent sky coverage,

$$\Omega_{S,i}\left(z\right) = \frac{\int_{L^i_{min}}^{L^i_{max}}\int_T \frac{\mathrm{d}n(L,T,z)}{\mathrm{d}L\,\mathrm{d}T}\Omega_S\left(L,T,z\right)\mathrm{d}T\mathrm{d}L}{\int_{L^i_{min}}^{L^i_{max}}\int_T \frac{\mathrm{d}n(L,T,z)}{\mathrm{d}L\,\mathrm{d}T}\mathrm{d}T\mathrm{d}L}, \tag{B.5}$$

where L^i_{min} and L^i_{max} are the boundaries of the luminosity bin i.

The luminosity function then reads

$$\frac{\mathrm{d}n}{\mathrm{d}L}(< L_i >) = \frac{1}{\Delta L_i}\frac{N_i}{V_i}, \tag{B.6}$$

where N_i is the total number of clusters in bin i and V_i the effective volume of the bin obtained from the sky coverage $\Omega_{S,i}$. We term this estimator the 'binned correction' method. The reduced noise in the correction of the sky coverage, compared to the point estimator, comes at the price of being slightly more model-dependent. However, the estimator only uses the shape of the luminosity function in the assumed model as a weight function, so it does not impose the measured luminosity function to match that of the model. In addition, since this estimator only becomes useful when the shot noise is high, the error on the underlying model would have to be very large to significantly bias the final result. Variants of this estimator are fairly common in the analysis of the luminosity function of X-ray AGNs (although expressed solely in terms of the AGN luminosity and redshift). For instance, Page & Carrera (2000) assumed $\mathrm{d}N/\mathrm{d}L\mathrm{d}z$ to be constant using narrow luminosity bins and showed the resulting estimator to be more robust than the simple point correction. For larger bins, Miyaji et al. (2001) used precisely the estimator of Eq. (B.6), having first derived $\mathrm{d}N/\mathrm{d}L\mathrm{d}z$ from a binned parametric fit to their data. Such recipes are meant to reduce the model dependence of the estimator. We did not try to implement them here as the modelled luminosity function already enters the determination of $\Omega_S\left(L,z\right)$.

When few clusters per bin are available, the shot noise can remain high, even with the binned correction, unless the luminosity function is smoothed over very wide luminosity bins. A possible alternative consists in directly measuring the cumulative luminosity function with a slight modification of Eq. (B.6):

$$n(> L) = \frac{N_{>L}}{V_{>L}}, \tag{B.7}$$

where $N_{>L}$ is the number of observed clusters above luminoity L, and $V_{>L}$ the bin averaged effective volume obtained by integrating the sky coverage of Eq. (B.5) to infinite luminosity. The differential luminosity function follows from differentiating Eq. (B.7). This is the 'cumulative correction' method that we use for the XXL-100-GC analysis. It is affected much less by

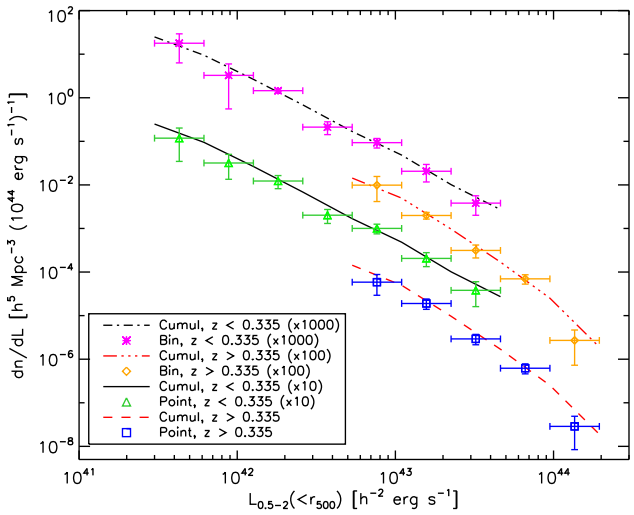

Fig. B.1. Comparison of the luminosity function obtained using the three estimators presented in Appendix B, in the fiducial WMAP9 cosmology, and scaling relation model. Multiplicative factors were added to separate the different estimates and to clarify the plot.

noise than the point and binned estimates, because the derivative uses the cluster density in several bins, implying that wider bins are effectively considered. However, this introduces correlations between the values of the luminosity function in adjacent bins. This would mostly be a problem while using the luminosity function directly to constrain physical cluster models or cosmological parameters. However, this is not desirable since the luminosity function estimate already relies on the assumed cosmology and cluster model to estimate the effective volume. For such analyses, one should instead adopt a likelihood formalism similar to the one presented in Appendix C and used in Sect. 6.3.

Naively, the sensitivity to the shape of the luminosity function in the assumed cosmological model should become even larger since the effective volume is averaged over a very wide luminosity bin. This would be true for the cumulative function of Eq. (B.7), but the effect is reduced in the case of the differential function because the derivative only results from finite differences of the cumulative function. This is confirmed by Monte Carlo computations of the luminosity function errors, which includes the uncertainty on the $L^{\rm XXL}_{500,MT} - T_{300\ \rm kpc}$ scaling relation (see Sect. 6.2) and yet produces smaller error bars for the cumulative correction method compared to others.

A comparison of the XXL-100-GC luminosity function obtained with these three estimators is provided in Fig. B.1, using large luminosity bins to reduce the shot noise in the point and binned corrrection method. All methods provide very similar values, justifying the use of the cumulative method which results in tighter constraints on the differential luminosity function.

Appendix C: Likelihood model

To infer model parameters ($\mathcal{P}$) from the properties of the XXL-100-GC clusters, we make use of a very generic unbinned likelihood model, in which we separate the information on the number of detected clusters, N_{det}, from their distribution in the space of observables (O),

$$\mathcal{L}(\mathcal{P}|N_{det},\tilde{O}) = P(N_{det}|\mathcal{P}) \prod_{i=1}^{N_{det}} \left[\int_O P(\tilde{O}|O) P(O|\mathcal{P}) \mathrm{d}O \right], \quad \text{(C.1)}$$

where $\tilde{O}$ are noisy measurements of the cluster observables (e.g. known redshifts, luminosities, and masses); $P(\tilde{O}|O)$ therefore describes the measurement process, while $P(O|\mathcal{P})$ is the expected distribution of the true observables O in the model described by parameters $\mathcal{P}$.

To proceed further, let us define the cluster density in the observable space, their redshift distribution, and the number of expected detections in model $\mathcal{P}$ as

$$\frac{\mathrm{d}N\,(L,T,z)}{\mathrm{d}z\,\mathrm{d}L\,\mathrm{d}T} = \frac{\mathrm{d}n\,(L,T,z)}{\mathrm{d}L\,\mathrm{d}T} \frac{\mathrm{d}^2V}{\mathrm{d}\Omega\,\mathrm{d}z} \Omega_S\,(L,T,z), \quad \text{(C.2)}$$

$$\frac{\mathrm{d}N}{\mathrm{d}z} = \int_L \int_T \frac{\mathrm{d}N\,(L,T,z)}{\mathrm{d}L\,\mathrm{d}T}\,\mathrm{d}L\,\mathrm{d}T, \quad \text{(C.3)}$$

$$\langle N_{det} \rangle = \int_z \frac{\mathrm{d}N}{\mathrm{d}z}\,\mathrm{d}z, \quad \text{(C.4)}$$

where $\mathrm{d}n/\mathrm{d}L\mathrm{d}T$ is the volumic cluster density defined by Eq. (6) and $\Omega_S\ (L,T,z)$ is the sky coverage of the survey as expressed in Eq. (B.2).

If only cluster temperatures, luminosities, and redshifts are considered, the predicted distribution of clusters in true observable space, present in Eq. (C.1), becomes

$$P(O|\mathcal{P}) = \frac{1}{\langle N_{det} \rangle} \frac{\mathrm{d}N\,(L,T,z)}{\mathrm{d}z\,\mathrm{d}L\,\mathrm{d}T}. \quad \text{(C.5)}$$

If, in addition, one assumes a Poisson distribution of mean $\langle N_{det} \rangle$ for $P(N_{det}|\mathcal{P})$, the likelihood becomes formally the same as the one defined by Mantz et al. (2010).

However, this new derivation makes explicit the contribution of the model normalisation, which allows for simple extensions to the basis model. For instance, for the fits to the cluster luminosity distribution performed in sections 6.3 and 7.3, we modified $P(N_{det}|\mathcal{P})$ to account for cosmic variance as

$$P(N_{det}|\mathcal{P}) = \int Poi(N_{det}|N_{loc}) \mathcal{LN}\,[N_{loc}|\langle N_{det} \rangle, \sigma_v]\ \mathrm{d}N_{loc} \quad \text{(C.6)}$$

where the local density N_{loc} is generated from a log-normal distribution $\mathcal{LN}$ of mean $\langle N_{det} \rangle$ and sample variance σ_v^2, and N_{loc} is then subjected to additional shot noise through the Poisson law Poi. Such log-normal models for the distribution of matter in the universe have already been used in several studies, starting with Coles & Jones (1991). We use the analytical model of Valageas et al. (2011) to compute the variance σ_v^2. In practice, we combined equations C.5 and C.6 with $P(\tilde{O}|O)$ arising from log-normal errors on the luminosity, unconstrained temperatures, and perfect redshift determinations for all the results presented in this article.

A second application of the present likelihood formalism is simply to ignore the information contained in the model normalisation by setting $P(N_{det}|\mathcal{P}) = 1$, as assumed in Paper III for the analysis of the scaling relations between luminosity and temperature. In this case, since the goal was to constrain the scaling relation without including any information from the spatial density of clusters, the redshift information was also ignored to consider only the raw distribution of $L^{\rm XXL}_{500,MT}$ and $T_{300\ \rm kpc}$ at given z. This implied

$$P(O|\mathcal{P}) = P(L,T|\mathcal{P},z) = \frac{1}{\mathrm{d}N/\mathrm{d}z} \frac{dN\,(L,T,z)}{dzdLdT}. \quad \text{(C.7)}$$

Appendix D: Additional tables

Table D.1. The Bright XXL cluster catalogue.

Name	RA	Dec	z	N_{gal}	C_{60}	F_{60}	$r_{500,\mathrm{MT}}$	$L^{\mathrm{XXL}}_{500,MT}$	$M_{500,\mathrm{MT}}$	Ref.
XLSSC 094	30.648	-6.732	0.886	3	199	4.82 ± 0.44	0.74	25.9 ± 2.2	⋆⋆	...
XLSSC 096	30.973	-5.027	0.520	6	161	3.64 ± 0.39	1.00	5.80 ± 0.62	48 ± 31	...
XLSSC 102	31.322	-4.652	0.969	3	199	4.20 ± 0.36	0.57	16.1 ± 1.7	19 ± 11	...
XLSSC 106	31.351	-5.732	0.300	14	681	9.13 ± 0.39	0.86	4.44 ± 0.21	24 ± 11	...
XLSSC 107	31.354	-7.594	0.436	3	263	5.58 ± 0.41	0.71	4.89 ± 0.41	15.9 ± 7.6	...
XLSSC 100	31.549	-6.193	0.915	6	124	3.55 ± 0.52	0.69	14.1 ± 3.2	26 ± 18	...
XLSSC 093	31.699	-6.948	0.429	6	418	7.23 ± 0.41	0.81	6.47 ± 0.42	23 ± 11	...
XLSSC 108	31.832	-4.827	0.254	4	451	6.16 ± 0.34	0.70	1.90 ± 0.13	12.7 ± 5.6	...
XLSSC 095	31.962	-5.206	0.138	12	141	3.09 ± 0.32	0.45	0.17 ± 0.03	2.9 ± 1.3	...
XLSSC 092	32.071	-7.276	0.432	3	166	3.14 ± 0.33	0.77	2.81 ± 0.31	20 ± 11	...
XLSSC 101	32.193	-4.436	0.756	9	332	5.49 ± 0.36	0.79	16.5 ± 1.3	31 ± 16	...
XLSSC 109	32.296	-6.346	0.491	2	146	5.11 ± 0.61	0.79	6.3 ± 1.0	23 ± 15	...
XLSSC 112	32.514	-5.462	0.139	14	178	5.89 ± 0.62	0.65	0.61 ± 0.08	9.0 ± 4.1	...
XLSSC 083	32.735	-6.200	0.430	5	293	4.68 ± 0.32	0.94	4.67 ± 0.38	37 ± 20	...
XLSSC 084	32.767	-6.211	0.430	6	173	3.28 ± 0.32	0.94	2.04 ± 0.31	36 ± 25	...
XLSSC 085	32.870	-6.196	0.428	3	206	4.09 ± 0.36	0.98	3.88 ± 0.40	$41 \pm 27^{**}$	...
XLSSC 111	33.111	-5.627	0.299	12	707	14.00 ± 0.57	1.02	6.65 ± 0.32	40 ± 18	...
XLSSC 098	33.115	-6.076	0.297	5	133	3.48 ± 0.42	0.80	1.73 ± 0.21	20 ± 12	...
XLSSC 099	33.220	-6.202	0.391	1	118	3.23 ± 0.39	1.03	2.26 ± 0.41	46 ± 40	...
XLSSC 097	33.342	-6.098	*0.76*	*0*	124	4.22 ± 0.48	0.79	13.4 ± 1.7	32 ± 19	...
XLSSC 110	33.537	-5.585	0.445	4	228	3.19 ± 0.28	0.53	1.63 ± 0.25	6.5 ± 2.8	14
XLSSC 060	33.668	-4.553	0.139	26	3553	23.03 ± 0.43	1.14	6.31 ± 0.08	47 ± 20	7, 11
XLSSC 072	33.850	-3.726	1.002	5	231	4.06 ± 0.36	0.61	14.9 ± 1.8	19 ± 11	6, 13
XLSSC 056	33.871	-4.682	0.348	6	532	7.55 ± 0.38	0.82	4.16 ± 0.25	22 ± 11	7
XLSSC 057	34.051	-4.242	0.153	18	463	8.01 ± 0.43	0.73	1.18 ± 0.07	12.9 ± 5.8	7, 11
XLSSC 023	35.188	-3.433	0.328	4	272	3.39 ± 0.28	0.66	1.63 ± 0.18	11.0 ± 5.2	4
XLSSC 006	35.439	-3.772	0.429	16	903	18.64 ± 0.71	0.98	17.42 ± 0.83	41 ± 18	2
XLSSC 061	35.485	-5.758	0.259	10	167	3.66 ± 0.40	0.68	1.09 ± 0.14	11.3 ± 5.8	7
XLSSC 036	35.527	-3.054	0.492	3	464	9.35 ± 0.49	0.80	11.14 ± 0.72	24 ± 11	4
XLSSC 029	36.017	-4.225	1.050	6	323	3.22 ± 0.23	0.63	19.5 ± 1.7	22 ± 12	3
XLSSC 062	36.061	-2.721	0.059	4	103	5.04 ± 0.69	0.42	0.11 ± 0.02	$2.3 \pm 1.0^{**}$	7
XLSSC 001	36.238	-3.817	0.614	17	522	6.43 ± 0.33	0.78	10.10 ± 0.72	25 ± 12	1
XLSSC 054	36.319	-5.887	0.054	28	421	7.76 ± 0.70	0.72	0.28 ± 0.02	11.3 ± 4.9	7
XLSSC 025	36.353	-4.680	0.265	13	680	6.55 ± 0.29	0.75	2.21 ± 0.11	15.5 ± 6.8	3
XLSSC 041	36.378	-4.239	0.142	16	454	12.54 ± 0.64	0.67	1.19 ± 0.07	9.7 ± 4.3	4
XLSSC 050	36.421	-3.189	0.140	16	782	9.79 ± 0.39	0.90	2.78 ± 0.07	23.3 ± 9.9	4
XLSSC 055	36.454	-5.896	0.232	14	464	7.81 ± 0.43	0.84	2.61 ± 0.15	21.2 ± 9.6	7
XLSSC 011	36.540	-4.969	0.054	42	349	3.23 ± 0.22	0.83	0.15 ± 0.01	17.1 ± 8.7	3
XLSSC 052	36.567	-2.666	0.056	3	599	9.03 ± 0.42	0.39	0.09 ± 0.01	1.70 ± 0.70	4
XLSSC 010	36.843	-3.362	0.330	6	308	4.60 ± 0.33	0.75	2.58 ± 0.21	16.6 ± 8.0	2
XLSSC 103	36.886	-5.961	0.233	8	164	4.27 ± 0.41	0.91	1.30 ± 0.14	27 ± 17	...
XLSSC 003	36.909	-3.300	0.836	6	163	3.40 ± 0.35	0.64	12.3 ± 1.5	19 ± 11	1
XLSSC 022	36.917	-4.858	0.293	18	1295	7.44 ± 0.23	0.67	3.06 ± 0.11	11.4 ± 4.8	3
XLSSC 027	37.012	-4.851	0.295	10	376	3.70 ± 0.23	0.77	1.48 ± 0.11	17.1 ± 8.1	4
XLSSC 090	37.121	-4.857	0.141	11	217	4.53 ± 0.37	0.51	0.43 ± 0.05	4.2 ± 1.8	...
XLSSC 089	37.127	-4.733	0.609	7	101	3.18 ± 0.40	0.77	6.44 ± 0.87	24 ± 18	...
XLSSC 104	37.324	-5.895	0.294	6	266	4.57 ± 0.34	1.04	1.36 ± 0.15	⋆⋆	...
XLSSC 088	37.611	-4.581	0.295	7	204	3.53 ± 0.31	0.73	1.57 ± 0.15	14.5 ± 7.7	...
XLSSC 087	37.720	-4.348	0.141	5	530	12.21 ± 0.59	0.62	0.92 ± 0.09	7.7 ± 3.2	...

Notes. Columns description: Name: Official IAU designation of the cluster. z: Cluster redshift. Photometric redshifts are only reported with two digit accuracy. RA/Dec: J2000 coordinates in degrees. N_{gal}: number of spectroscopic redshifts for cluster members - 0 means that only photometric redshits are available C_{60}: Net XMM counts in the [0.5-2] keV band within the 60″ aperture used for the sample selection. F_{60}: Flux in the [0.5-2] keV band within the 60″ aperture, in units of 10^{-14} erg s^{-1} cm^{-2}. $r_{500,\mathrm{MT}}$: Overdensity radius with respect to the critical density in Mpc, obtained from the $M_{500,\mathrm{WL}} - T_{300\ \mathrm{kpc}}$ scaling relation of Paper IV (see Table 1) and the temperatures measured in Paper III. $L^{\mathrm{XXL}}_{500,MT}$: Rest-frame [0.5-2] keV luminosity in $r_{500,\mathrm{MT}}$ in units of 10^{43} erg s^{-1}. $M_{500,\mathrm{MT}}$: mass within $r_{500,\mathrm{MT}}$ in units of $10^{13}\ M_{\odot}$, obtained from the $M_{500,\mathrm{WL}} - T_{300\ \mathrm{kpc}}$ scaling relation of Paper IV (see Table 1) and the temperatures measured in Paper III. A ** sign after the mass indicates a possible AGN contamination and thus a likely overestimated mass. We do not provide a mass for clusters that show firm evidence of AGN contaminations (although $r_{500,MT}$ was still derived from T_{300kpc} using the scaling relation of Paper IV). These clusters are indicated by a ⋆⋆ sign. Ref.: reference to first X-ray detection (as a cluster, when possible). A reference to the first optical/IR detection is also provided when it is prior to the X-ray detection.

References. (1) Valtchanov et al. (2004); (2) Willis et al. (2005); (3) Pierre et al. (2006); (4) Pacaud et al. (2007); (5) Adami et al. (2011); (6) Willis et al. (2013); (7) Clerc et al. (2014); (8) Šuhada et al. (2012); (9) Böhringer et al. (2004); (10) Voges et al. (2000); (11) Abell et al. (1989); (12) Menanteau et al. (2010); (13) Muzzin et al. (2012); (14) Limousin et al. (2009); (15) Jones et al. (2009).

Table D.1. continued.

Name	RA	Dec	z	N_{gal}	C_{60}	F_{60}	$r_{500,\mathrm{MT}}$	$L^{\mathrm{XXL}}_{500,MT}$	$M_{500,\mathrm{MT}}$	Ref.
XLSSC 091	37.926	-4.881	0.186	41	3114	38.65 ± 0.72	1.15	13.12 ± 0.19	51 ± 22	11
XLSSC 105	38.411	-5.506	0.429	5	543	12.87 ± 0.64	1.02	12.39 ± 0.89	47 ± 24	...
XLSSC 502	348.442	-53.438	0.141	4	442	6.52 ± 0.37	0.53	0.63 ± 0.05	4.9 ± 2.0	...
XLSSC 530	348.833	-54.345	*0.18*	*0*	332	4.47 ± 0.32	0.69	0.75 ± 0.06	10.9 ± 4.9	...
XLSSC 501	348.873	-53.063	0.333	7	265	6.01 ± 0.49	0.77	2.44 ± 0.29	17.8 ± 9.1	...
XLSSC 513	349.221	-54.902	0.378	5	409	11.19 ± 0.65	0.94	6.50 ± 0.44	34 ± 17	8, 12
XLSSC 525	349.339	-53.962	0.379	2	904	10.53 ± 0.39	0.83	6.68 ± 0.33	24 ± 10	...
XLSSC 527	349.570	-55.984	0.076	3	100	4.80 ± 0.62	0.93	0.20 ± 0.05	24 ± 27	...
XLSSC 528	349.682	-56.204	0.302	5	427	4.28 ± 0.25	0.84	2.07 ± 0.16	23 ± 12	...
XLSSC 529	349.699	-56.287	0.547	6	398	5.02 ± 0.30	0.77	6.91 ± 0.58	23 ± 11	12
XLSSC 526	349.802	-54.087	0.273	8	55	15.33 ± 3.06	0.79	5.27 ± 0.27	18.5 ± 8.3	10, 11
XLSSC 544	349.816	-53.534	0.095	11	927	10.52 ± 0.40	0.79	0.77 ± 0.03	15.2 ± 6.6	...
XLSSC 518	349.822	-55.325	0.177	4	453	6.34 ± 0.39	0.53	0.58 ± 0.05	5.1 ± 2.1	8
XLSSC 531	349.876	-56.649	0.391	9	190	3.65 ± 0.36	0.97	2.73 ± 0.38	38 ± 30	12
XLSSC 534	350.105	-53.359	0.853	4	154	3.53 ± 0.40	0.73	16.1 ± 2.4	27 ± 18	...
XLSSC 517	350.449	-55.971	0.699	3	155	4.07 ± 0.46	0.70	7.3 ± 1.1	20 ± 12	...
XLSSC 523	350.503	-54.750	0.343	7	223	5.03 ± 0.41	0.78	2.90 ± 0.23	18.8 ± 9.5	8, 11
XLSSC 503	350.646	-52.747	0.336	3	230	4.92 ± 0.43	0.64	2.47 ± 0.24	10.5 ± 4.9	...
XLSSC 545	350.692	-53.388	0.353	7	100	3.09 ± 0.46	0.67	1.41 ± 0.41	12 ± 11	...
XLSSC 514	351.396	-54.722	0.169	9	229	3.99 ± 0.37	0.58	0.47 ± 0.07	6.6 ± 3.0	8, 12
XLSSC 515	351.416	-54.741	0.101	11	350	5.75 ± 0.40	0.54	0.37 ± 0.04	4.9 ± 2.1	8, 12
XLSSC 547	351.427	-53.277	0.371	6	164	5.32 ± 0.52	0.92	4.09 ± 0.40	32 ± 18	...
XLSSC 535	351.554	-53.317	0.172	11	607	11.61 ± 0.54	0.76	2.41 ± 0.13	14.4 ± 6.5	12
XLSSC 536	351.557	-53.374	0.170	7	282	6.28 ± 0.47	0.66	0.47 ± 0.08	9.5 ± 4.5	...
XLSSC 522	351.638	-55.022	0.395	3	819	3.63 ± 0.17	0.71	2.71 ± 0.19	15.2 ± 7.0	8, 12
XLSSC 533	351.712	-52.694	0.107	6	1315	18.10 ± 0.55	0.79	2.21 ± 0.05	15.4 ± 6.5	9
XLSSC 504	351.930	-52.425	0.243	1	150	5.13 ± 0.67	1.95	1.35 ± 0.48	★★	...
XLSSC 521	352.179	-55.567	0.807	1	281	6.66 ± 0.50	0.78	17.3 ± 1.9	31 ± 18	8
XLSSC 505	352.250	-52.238	0.055	3	545	19.22 ± 0.95	0.66	0.47 ± 0.03	8.6 ± 3.7	...
XLSSC 506	352.315	-52.497	0.717	6	95	3.05 ± 0.54	0.80	8.5 ± 1.7	31 ± 24	12
XLSSC 546	352.416	-53.249	0.792	2	256	3.67 ± 0.30	0.67	13.1 ± 1.4	20 ± 10	...
XLSSC 512	352.484	-56.136	0.402	3	458	3.25 ± 0.20	0.85	2.99 ± 0.19	26 ± 12	8
XLSSC 520	352.502	-54.619	0.175	7	1338	12.66 ± 0.38	0.81	2.34 ± 0.07	17.4 ± 7.4	8, 12
XLSSC 532	352.948	-52.669	0.392	5	375	4.92 ± 0.30	0.77	3.43 ± 0.31	19.4 ± 9.8	...
XLSSC 519	353.019	-55.212	0.270	3	155	4.11 ± 0.46	0.56	0.94 ± 0.18	6.3 ± 2.9	8
XLSSC 524	353.067	-54.702	0.270	8	264	3.38 ± 0.28	0.75	1.21 ± 0.12	15.8 ± 8.0	8, 12
XLSSC 542	353.113	-53.976	0.402	2	3038	46.76 ± 0.88	1.20	50.4 ± 1.1	74 ± 32	10, 12
XLSSC 507	353.374	-52.252	0.566	6	144	3.93 ± 0.47	0.61	4.43 ± 0.76	11.7 ± 6.5	12
XLSSC 549	353.515	-53.141	0.808	3	201	3.33 ± 0.31	0.71	11.3 ± 1.9	24 ± 20	...
XLSSC 516	353.881	-54.586	*0.87*	*0*	189	3.13 ± 0.33	0.70	23.3 ± 2.5	29 ± 15	8
XLSSC 537	354.029	-53.876	0.515	12	348	5.54 ± 0.36	0.93	8.07 ± 0.67	39 ± 21	12
XLSSC 548	354.193	-53.793	0.321	3	175	3.09 ± 0.33	0.43	0.51 ± 0.13	3.0 ± 1.3	...
XLSSC 538	354.646	-54.623	0.332	4	276	3.39 ± 0.26	0.80	1.83 ± 0.19	20 ± 12	...
XLSSC 543	354.863	-55.843	0.381	2	199	3.35 ± 0.32	0.69	1.33 ± 0.18	13.6 ± 7.0	...
XLSSC 541	355.431	-55.965	0.188	6	415	6.77 ± 0.40	0.81	1.42 ± 0.09	17.7 ± 8.0	...
XLSSC 508	355.465	-53.145	0.539	2	498	9.80 ± 0.50	0.74	4.55 ± 0.43	20 ± 11	12
XLSSC 540	355.632	-56.353	0.414	9	483	6.53 ± 0.36	0.78	5.52 ± 0.34	20.1 ± 9.3	...
XLSSC 539	355.797	-55.881	0.184	2	195	3.78 ± 0.39	0.52	0.44 ± 0.08	4.7 ± 2.2	...
XLSSC 509	356.461	-54.044	0.633	12	186	3.70 ± 0.36	0.81	8.99 ± 0.86	29 ± 17	...
XLSSC 510	357.539	-55.334	0.394	1	380	3.93 ± 0.26	0.71	2.96 ± 0.20	15.2 ± 7.2	...
XLSSC 511	357.753	-55.371	0.130	3	247	3.50 ± 0.28	0.54	0.29 ± 0.04	5.2 ± 2.2	...

Table D.2. Supplementary clusters to the XXL-100-GC sample catalogue.

Name	RA	Dec	z	N_{gal}	C_{60}	F_{60}	$r_{500,\mathrm{MT}}$	$L^{\mathrm{XXL}}_{500,MT}$	$M_{500,\mathrm{MT}}$	Ref.
XLSSC 114	30.425	-5.031	0.234	6	91	3.51 ± 0.76	1.07	1.59 ± 0.30	44 ± 51	...
XLSSC 113	30.561	-7.009	0.050	9	340	11.47 ± 0.80	0.56	0.37 ± 0.03	$5.2 \pm 2.2^{**}$	...
XLSSC 115	32.681	-6.588	0.043	22	156	12.21 ± 1.31	0.74	0.68 ± 0.05	12.1 ± 6.8	...
XLSSC 550	352.206	-52.577	0.109	3	156	8.77 ± 1.06	0.48	0.32 ± 0.06	3.4 ± 1.5	...
XLSSC 551	355.444	-56.675	0.475	4	189	4.66 ± 0.54	0.67	3.96 ± 0.67	13.7 ± 7.9	...
XLSSC 118	33.692	-3.941	0.140	1	5144	78.77 ± 1.17	0.63	6.92 ± 0.15	★★	15
XLSSC 552	350.629	-54.269	0.152	1	3592	57.93 ± 0.98	0.75	6.81 ± 0.12	$13.8 \pm 5.8^{**}$	12, 8

Notes. These clusters are above the flux limit required for inclusion in the main sample, but failed to comply with other requirements. The five clusters above the horizontal line were detected in "bad" pointings according to the nominal thresholds on the background level and exposure time, while the two clusters below the line were not part of the pipeline C1+C2 selection. The table layout is the same as in Table D.1.

References

Abell, G. O., Corwin, Jr., H. G., & Olowin, R. P. 1989, ApJS, 70, 1
Adami, C., Mazure, A., Pierre, M., et al. 2011, A&A, 526, A18
Alshino, A., Ponman, T., Pacaud, F., & Pierre, M. 2010, MNRAS, 407, 2543
Batuski, D. J. & Burns, J. O. 1985, AJ, 90, 1413
Benson, B. A., de Haan, T., Dudley, J. P., et al. 2013, ApJ, 763, 147
Bertin, E. & Arnouts, S. 1996, A&AS, 117, 393
Bleem, L. E., Stalder, B., de Haan, T., et al. 2015, ApJS, 216, 27
Böhringer, H., Chon, G., & Collins, C. A. 2014, A&A, 570, A31
Böhringer, H., Schuecker, P., Guzzo, L., et al. 2004, A&A, 425, 367
Böhringer, H., Schuecker, P., Guzzo, L., et al. 2001, A&A, 369, 826
Böhringer, H., Voges, W., Huchra, J. P., et al. 2000, ApJS, 129, 435
Burenin, R. A., Vikhlinin, A., Hornstrup, A., et al. 2007, ApJS, 172, 561
Cavaliere, A. & Fusco-Femiano, R. 1976, A&A, 49, 137
Chon, G., Böhringer, H., & Nowak, N. 2013, MNRAS, 429, 3272
Chow-Martínez, M., Andernach, H., Caretta, C. A., & Trejo-Alonso, J. J. 2014, MNRAS, 445, 4073
Clerc, N., Adami, C., Lieu, M., et al. 2014, MNRAS, 444, 2723
Clerc, N., Sadibekova, T., Pierre, M., et al. 2012, MNRAS, 423, 3561
Coles, P. & Jones, B. 1991, MNRAS, 248, 1
Driver, S. P., Hill, D. T., Kelvin, L. S., et al. 2011, MNRAS, 413, 971
Ebeling, H., Edge, A. C., & Henry, J. P. 2001, ApJ, 553, 668
Einasto, J., Einasto, M., Tago, E., et al. 2007, A&A, 462, 811
Einasto, M., Einasto, J., Tago, E., Müller, V., & Andernach, H. 2001, AJ, 122, 2222
Einasto, M., Lietzen, H., Tempel, E., et al. 2014, A&A, 562, A87
Eisenstein, D. J. & Hu, W. 1999, ApJ, 511, 5
Erben, T., Hildebrandt, H., Miller, L., et al. 2013, MNRAS, 433, 2545
Fassbender, R., Böhringer, H., Nastasi, A., et al. 2011, New Journal of Physics, 13, 125014
Finoguenov, A., Guzzo, L., Hasinger, G., et al. 2007, ApJS, 172, 182
Gal, R. R. & Lubin, L. M. 2004, ApJ, 607, L1
Garilli, B., Guzzo, L., Scodeggio, M., et al. 2014, A&A, 562, A23
Giles, P. A., Maughan, B. J., Pacaud, P., et al. 2016, A&A, in press (XXL Survey, III)
Gioia, I. M., Maccacaro, T., Schild, R. E., et al. 1990, ApJS, 72, 567
Gregory, P. C., Vavasour, J. D., Scott, W. K., & Condon, J. J. 1994, ApJS, 90, 173
Hamilton, A. J. S. 1993, ApJ, 417, 19
Helsdon, S. F. & Ponman, T. J. 2000, MNRAS, 315, 356
Henning, J. W., Gantner, B., Burns, J. O., & Hallman, E. J. 2009, ApJ, 697, 1597
Henry, J. P., Gioia, I. M., Maccacaro, T., et al. 1992, ApJ, 386, 408
Henry, J. P., Mullis, C. R., Voges, W., et al. 2006, ApJS, 162, 304
Hinshaw, G., Larson, D., Komatsu, E., et al. 2013, ApJS, 208, 19
Hoekstra, H., Herbonnet, R., Muzzin, A., et al. 2015, MNRAS, 449, 685
Hog, E., Kuzmin, A., Bastian, U., et al. 1998, A&A, 335, L65
Jones, D. H., Read, M. A., Saunders, W., et al. 2009, MNRAS, 399, 683
Kaiser, N. 1986, MNRAS, 222, 323
Kalberla, P. M. W., Burton, W. B., Hartmann, D., et al. 2005, A&A, 440, 775
Kalinkov, M. & Kuneva, I. 1995, A&AS, 113, 451
Koens, L. A., Maughan, B. J., Jones, L. R., et al. 2013, MNRAS, 435, 3231
Koulouridis, E., Poggianti, B., Altieri, B., et al. 2016, A&A, in press (XXL Survey, XII)
Kuntz, K. D. & Snowden, S. L. 2008, A&A, 478, 575
Landy, S. D. & Szalay, A. S. 1993, ApJ, 412, 64
Le Fèvre, O., Cassata, P., Cucciati, O., et al. 2013, A&A, 559, A14
Lidman, C., Ardila, F., Owers, M., et al. 2016, PASA, in press (XXL Survey, XIV)
Lieu, M., Smith, G. P., Giles, P. A., et al. 2016, A&A, in press (XXL Survey, IV)
Limousin, M., Cabanac, R., Gavazzi, R., et al. 2009, A&A, 502, 445
Mantz, A., Allen, S. W., Ebeling, H., & Rapetti, D. 2008, MNRAS, 387, 1179
Mantz, A., Allen, S. W., Rapetti, D., & Ebeling, H. 2010, MNRAS, 406, 1759
Mantz, A. B., von der Linden, A., Allen, S. W., et al. 2015, MNRAS, 446, 2205
Mehrtens, N., Romer, A. K., Hilton, M., et al. 2012, MNRAS, 423, 1024
Menanteau, F., Hughes, J. P., Barrientos, L. F., et al. 2010, ApJS, 191, 340
Miyaji, T., Hasinger, G., & Schmidt, M. 2001, A&A, 369, 49
Mocanu, L. M., Crawford, T. M., Vieira, J. D., et al. 2013, ApJ, 779, 61
Moretti, A., Lazzati, D., Campana, S., & Tagliaferri, G. 2002, ApJ, 570, 502
Mullis, C. R., Vikhlinin, A., Henry, J. P., et al. 2004, ApJ, 607, 175
Muzzin, A., Wilson, G., Yee, H. K. C., et al. 2012, ApJ, 746, 188
Nord, B., Stanek, R., Rasia, E., & Evrard, A. E. 2008, MNRAS, 383, L10
Pacaud, F., Pierre, M., Adami, C., et al. 2007, MNRAS, 382, 1289
Pacaud, F., Pierre, M., Refregier, A., et al. 2006, MNRAS, 372, 578
Page, M. J. & Carrera, F. J. 2000, MNRAS, 311, 433
Peebles, P. J. E. & Hauser, M. G. 1974, ApJS, 28, 19
Piccinotti, G., Mushotzky, R. F., Boldt, E. A., et al. 1982, ApJ, 253, 485
Pierre, M., Chiappetti, L., Pacaud, F., et al. 2007, MNRAS, 382, 279
Pierre, M., Pacaud, F., Adami, C., et al. 2016, A&A, in press (XXL Survey, I)
Pierre, M., Pacaud, F., Duc, P.-A., et al. 2006, MNRAS, 372, 591
Pierre, M., Pacaud, F., Juin, J. B., et al. 2011, MNRAS, 414, 1732
Planck Collaboration, Ade, P. A. R., Aghanim, N., et al. 2014, A&A, 571, A20
Planck Collaboration, Ade, P. A. R., Aghanim, N., et al. 2011, A&A, 536, A1
Planck Collaboration, Ade, P. A. R., Aghanim, N., et al. 2015a, ArXiv e-prints, 1502.01598
Planck Collaboration, Ade, P. A. R., Aghanim, N., et al. 2015b, ArXiv e-prints, arXiv:1502.01589
Planck Collaboration, Ade, P. A. R., Aghanim, N., et al. 2015c, ArXiv e-prints, arXiv:1502.01597
Pompei, E., Adami, C., Eckert, D., et al. 2016, A&A, in press (XXL Survey, VII)
Pratt, G. W. & Arnaud, M. 2002, A&A, 394, 375
Read, A. M. & Ponman, T. J. 2003, A&A, 409, 395
Romer, A. K., Viana, P. T. P., Liddle, A. R., & Mann, R. G. 2001, ApJ, 547, 594
Rosati, P., Borgani, S., & Norman, C. 2002, ARA&A, 40, 539
Rosati, P., Della Ceca, R., Norman, C., & Giacconi, R. 1998, ApJ, 492, L21
Rozo, E., Wechsler, R. H., Rykoff, E. S., et al. 2010, ApJ, 708, 645
Sadibekova, T., Pierre, M., Clerc, N., et al. 2014, A&A, 571, A87
Sahlén, M., Viana, P. T. P., Liddle, A. R., et al. 2009, MNRAS, 397, 577
Scoville, N., Aussel, H., Brusa, M., et al. 2007, ApJS, 172, 1
Sehgal, N., Trac, H., Acquaviva, V., et al. 2011, ApJ, 732, 44
Stanek, R., Evrard, A. E., Böhringer, H., Schuecker, P., & Nord, B. 2006, ApJ, 648, 956
Starck, J.-L. & Pierre, M. 1998, A&AS, 128, 397
Tinker, J., Kravtsov, A. V., Klypin, A., et al. 2008, ApJ, 688, 709
Truemper, J. 1993, Science, 260, 1769
Ueda, Y., Watson, M. G., Stewart, I. M., et al. 2008, ApJS, 179, 124
Šuhada, R., Song, J., Böhringer, H., et al. 2012, A&A, 537, A39
Valageas, P., Clerc, N., Pacaud, F., & Pierre, M. 2011, A&A, 536, A95
Valtchanov, I., Pierre, M., Willis, J., et al. 2004, A&A, 423, 75
Vikhlinin, A., Kravtsov, A. V., Burenin, R. A., et al. 2009, ApJ, 692, 1060
Voges, W., Aschenbach, B., Boller, T., et al. 2000, IAU Circ., 7432, 1
Weinberg, D. H., Mortonson, M. J., Eisenstein, D. J., et al. 2013, Phys. Rep., 530, 87
Willis, J. P., Clerc, N., Bremer, M. N., et al. 2013, MNRAS, 430, 134
Willis, J. P., Pacaud, F., Valtchanov, I., et al. 2005, MNRAS, 363, 675

[1] Argelander-Institut für Astronomie, University of Bonn, Auf dem Hügel 71, D-53121 Bonn, Germany
e-mail: fpacaud@astro.uni-bonn.de
[2] Max-Planck-Institut für Extraterrestrische Physik, Giessenbachstraße, D-85748 Garching bei München, Germany
[3] H.H. Wills Physics Laboratory, University of Bristol, Tyndall Avenue, Bristol, BS8 1TL, UK
[4] Aix-Marseille Université, CNRS, LAM (Laboratoire d'Astrophysique de Marseille) UMR 7326 13388, Marseille, France
[5] Service d'Astrophysique AIM, CEA/DSM/IRFU/SAp, CEA Saclay, F-91191 Gif sur Yvette France
[6] School of Physics and Astronomy, University of Birmingham, Birmingham B15 2TT, UK
[7] Service d'Électronique des Détecteurs et d'Informatique, CEA/DSM/IRFU/SEDI, CEA Saclay, F-91191 Gif-sur-Yvette, France
[8] Department of Astronomy and Space Sciences, Faculty of Science, Istanbul University, 34119 Istanbul, Turkey
[9] Laboratoire Lagrange, UMR 7293, Université de Nice Sophia Antipolis, CNRS, Observatoire de la Côte d'Azur, F-06304 Nice, France
[10] European Space Astronomy Centre, ESA, P.O. Box 78, E-28691 Villanueva de la Cañada, Madrid, Spain
[11] Department of Astronomy, University of Florida, Gainesville, FL 32611, USA
[12] INAF, IASF Milano, via Bassini 15, I-20133 Milano, Italy
[13] Department of Astronomy, University of Geneva, ch. d'Écogia 16, CH-1290, Versoix, Switzerland
[14] Departments of Physics and Astronomy, and Michigan Center for Theoretical Physics, University of Michigan, Ann Arbor, MI 48109 USA
[15] Astrophysics and Cosmology Research Unit, University of KwaZulu-Natal, Durban, 4041, South Africa
[16] Australian Astronomical Observatory, PO BOX 915, North Ryde, 1670, Australia
[17] Department of Earth and Space Sciences, Onsala Space Observatory, Chalmers University of Technology, SE-439 92 Onsala, Sweden
[18] INAF - Osservatorio Astronomico di Brera, Via Brera 28, I-20122 Milano & via E. Bianchi 46, I-23807 Merate, Italy
[19] Institute for Astronomy & Astrophysics, Space Applications & Remote Sensing, National Observatory of Athens, GR-15236 Palaia Penteli, Athens, Greece
[20] National Center for Supercomputing Applications and Department of Astronomy University of Illinois at Urbana-Champaign, Urbana, IL 61801, USA
[21] Department of Physics and Astronomy, Macquarie University, Sydney NSW 2109, Australia
[22] INAF - Osservatorio Astronomico di Padova, Vicolo dell'Osservatorio, 5, I-35122, Padova, Italy
[23] European Southern Observatory, Alonso de Cordova 3107, Casilla 19001, Vitacura, Santiago de Chile, Chile
[24] Dark Cosmology Centre, Niels Bohr Institute, University of Copenhagen, Juliane Maries Vej 30, DK-2100 Copenhagen, Denmark
[25] Faculty of Physics, Ludwig-Maximilians University, Scheinerstrasse 1, D-81679 Munich, Germany
[26] Institut de Physique Théorique, CEA/DSM/IPhT and CNRS/URA 2306, F-91191 Gif-sur-Yvette, Cédex, France
[27] Department of Physics and Astronomy, University of Victoria, 3800 Finnerty Road, Victoria, BC, Canada
[28] Astrophysics Research Institute, Liverpool John Moores University, IC2, Liverpool Science Park, 146 Brownlow Hill, Liverpool L3 5RF, UK
[29] ESO, Karl-Schwarzschild-Str. 2 D-85748 Garching bei München Germany
[30] Astrophysics Department Max Planck Institut für Kernphysik Saupfercheckweg 1 D-69117 Heidelberg Germany